

Dynamic mechanical properties and fracturing behaviour of concrete under biaxial compression

H.C. Wang^a, J. Zhao^a, Jing Li^{a,*}, Kai Liu^b, C.H. Braithwaite^c, Q.B. Zhang^a

^a Department of Civil Engineering, Monash University, VIC 3800, Australia

^b Department of Engineering Science, University of Oxford, Oxford, OX1 3PJ, United Kingdom.

^c Cavendish Laboratory, JJ Thomson Avenue, Cambridge CB3 0HE, United Kingdom.

*Corresponding author: Jing.li2@monash.edu; Tel. +61 4523 20917

Abstract

Heterogeneity is an important factor affecting the dynamic mechanical properties and failure process of geomaterials especially when considering the coupled effect of strain rates and confinements. In this research, dynamic biaxial compression tests are conducted on concrete by using a triaxial Hopkinson bar system with different biaxial confinements (i.e., pre-stress σ_1 and σ_2 : 5~30 MPa) and impact velocities (i.e., 14~18 m/s). High-speed three-dimensional digital image correlation (3D-DIC), synchrotron-based micro-computed-tomography (micro-CT) and a machine learning-based crack classification technique are adopted to quantify the dynamic deformation and fracturing properties. Experimental results show that both dynamic strength and peak strain decrease with the increase of axial pre-stress σ_1 , but increase with increasing lateral pre-stress σ_2 and impact velocity. Fractures generally propagate from the surfaces of the specimen towards the centre along the impact direction, and appear at interfaces and in the matrix first and aggregates afterwards. Real-time surface deformation and post-failure fractures are aggravated with pre-stress σ_1 and impact velocity, but restrained by pre-stress σ_2 . Statistical crack analysis indicates that different crack types (e.g., matrix crack, interfacial crack and transgranular crack) own distinct geometrical characteristics (e.g., orientation distribution, fractal dimension and position distribution) and are affected by the orientation and aspect ratio of aggregate. Moreover, transgranular crack ratio decreases with higher pre-stress σ_1 , but increases with larger pre-stress σ_2 and impact velocity, consistent with variation of total stress and fracture energy, implying the significance of transgranular crack on mechanical properties and fracture energy of heterogeneous geomaterials under dynamic loadings.

Keywords: Concrete; Biaxial confinement; Strain rate; Dynamic failure; Microcrack statistics

1. Introduction

Geomaterials like concrete and rock have been widely used and existed in a variety of engineering fields, such as civil engineering, hydraulic projects and mining activities, where they are subjected to dynamic and extreme loadings, from natural disasters (e.g., earthquake, landslide, hurricane and tsunami) and human-induced hazards (e.g., rock blast, incidental impacts, accidental explosions and terrorist attacks) [1-3]. At the same time, geomaterials may encounter multiaxial stress states in engineering structures (e.g., beam-column joints, tunnel shells, nuclear power stations and dams) in civil and hydraulic engineering [4, 5], and in rock masses with *in-situ* stresses of more than 30 MPa in mining projects [6, 7]. Under dynamic loading, structures and rock masses (especially under biaxial stress states) are more likely to deteriorate and collapse, causing great loss of property and human life [8, 9]. In addition, heterogeneity, as an inherent characteristic of natural and artificial geomaterials from macroscopic to microscopic [10-12] shown in Fig. 1, has an important effect on the strength, deformation and fracturing process of geomaterials [13-15]. For example, an increase in heterogeneity will generally reduce the strength and induce post-peak ductile deformation according to numerical modelling [16]. In addition, multiple crack types (e.g., intergranular and transgranular crack) controlled by heterogeneous structures in natural rocks have been observed and analysed at a microscale level [17]. However, for rocks, investigations into heterogeneity are mainly conducted by numerical modelling. The heterogeneous structures (e.g., mineral type, grain size, and anisotropic crystal shape) are hard to be controlled in experiments, and the microcrack statistics of large-scale specimens are still challenging. Compared with rocks, concretes with heterogeneous structures (e.g., types, sizes and shapes of aggregates) are relatively easy to be studied [18, 19], and their multiple crack patterns (e.g., matrix cracks, interfacial cracks and transgranular cracks) can be obviously identified. Thus, concrete is an ideal material for an experimental study investigating the confinement effect and strain rate effect.

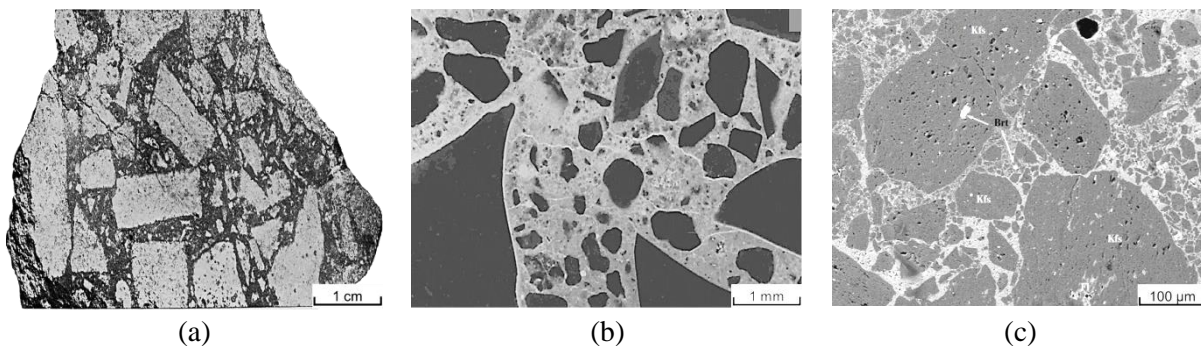


Fig. 1. Heterogeneous geomaterials: (a) Mineralised quartz monzonite breccia in Cactus mine in ore deposits of Utah [10], (b) fluorescence microscopy of concrete specimens [11] and (c) Trachyte breccia with barite-fluorite cement in SEM image [12].

Various experimental studies have been conducted on mechanical properties of geomaterials under multiaxial loadings with strain rates from 10^{-5} to 10^3 s^{-1} [20-22]. The multiaxial confinement loadings can be classified into three types, including conventional triaxial compression (type I: $\sigma_1 > \sigma_2 = \sigma_3 > 0$), true triaxial compression (type II: $\sigma_1 > \sigma_2 > \sigma_3 > 0$) and biaxial compression (type III: $\sigma_1 > \sigma_2 > \sigma_3 = 0$) as summarised in Table 1. Conventional

triaxial loadings include active confinements (e.g., hydraulic confinements and coupling static-dynamic loadings) combining the split Hopkinson pressure bar (SHPB) or universal loading machines with hydraulic pressure cells [23-31], and passive confinements by means of SHPB with cylindrical jacketing (e.g., shrink-fit metal sleeve and thick confining vessel) [31-36], but the confinement is isotropic without considering the effect of deviator stress. To overcome this deficiency, servo-hydraulic triaxial systems can be applied to achieve true triaxial loadings [37-39], but their strain rates are relatively low. Although drop-weight facilities combined with the biaxial hydraulic machine has been designed to realise impact tests, there are several challenges to be considered, such as stress equilibrium and controlled strain rate [40]. To replicate *in-situ* biaxial loading conditions, different techniques have been adopted, for example, tangential loading techniques [41], servo-hydraulic confinements [5, 42-45], a biaxial dynamic compression system [46] and coupled static-dynamic loading systems [47, 48]. Mechanical properties (e.g., stress-strain curves, peak strength and strain rate effect) of geomaterials under biaxial loadings have been studied, but the tests are mainly at low strain rates. Recently, a triaxial Hopkinson bar (Tri-HB) system has been developed by combining SHPB with a triaxial hydraulic loading system, which could realise true triaxial loadings and high strain rates [49, 50]. Although some geomaterials have been studied using the Tri-HB system [51-54], the mechanical behaviour of concrete under biaxial stress states and high strain rates is still unclear. Furthermore, concretes under biaxial loadings are relatively dangerous in engineering fields due to the weak mechanical properties compared with triaxial. The fracturing process and post-failure patterns are various under different loading conditions [55, 56], which has to be quantitatively analysed. Investigating the mechanical properties and fracturing behaviour of concrete under biaxial confinements and dynamic loadings can provide valuable information, such as calibration of constitutive models, clarification of fracture processes, and explanations of failure mechanisms.

Table 1. Studies on dynamic behaviours of geomaterials under multiaxial loadings.

| Confinement types | Loading facility | Materials | Confining pressure (MPa) | Strain rate $\dot{\epsilon}$ (s ⁻¹) | Main outcomes | Reference |
|---|-------------------------|-----------|--------------------------|---|---|-----------|
| I. $\sigma_1 > \sigma_2 = \sigma_3 > 0$, Conventional triaxial compression (CTC) | | | | | | |
| Hydraulic confinement | SHPB | Sandstone | 95 | 10 ² -10 ³ | Stress-strain relationship | [23] |
| | SHPB | Basalt | 100 | 10 ² -10 ³ | Strain rate dependence; Fracture properties | [24] |
| | 4-kbar loader | Concrete | 124 | 10 ⁻³ -10 ⁻¹ | Stress-strain curve; Strain rate dependence | [25] |
| | SHPB | Concrete | 4 | 10 ¹ -10 ² | Stress-strain relationship | [26] |
| | Servo-hydraulic machine | Concrete | 94 | 10 ⁻⁵ -10 ¹ | Strain rate sensitivity | [27] |
| | SHPB | Granite | 10 | 10 ¹ -10 ² | Confinement effect; Strain rate dependence | [29] |
| | SHPB | Marble | 10 | 10 ¹ -10 ² | Strain rate sensitivity; Confinement effect | [31] |
| Coupling static-dynamic loading | SHPB | Siltstone | 200 | 10 ⁻² -10 ² | Strength characteristics | [28] |
| | SHPB | Sandstone | 40 | 10 ¹ -10 ² | Failure mode; Cyclic loading | [30] |
| Shrink-fit metal sleeve | SHPB | Concrete | 17.5 | 10 ² -10 ³ | Dynamic strength; Confinement coefficient | [34] |
| | SHPB | Granite | 132 | 10 ² -10 ³ | Strain rate sensitivity; B-D transition | [35] |

Dynamic mechanical properties and fracturing behaviour of concrete under biaxial compression

| | | | | | | |
|--|-----------------------------------|---------------------|------|-----------------------|---|------|
| Thick confining vessel | SHPB | Aggregate composite | 265 | 10^1 - 10^3 | Confinement effect; Strain rate effect | [36] |
| | SHPB | Concrete | 45 | 10^1 - 10^2 | Severe deformation at the beginning period | [32] |
| | SHPB | Concrete | 550 | 10^1 - 10^2 | Dynamic strength; Strain rate dependence | [33] |
| | SHPB | Marble | 15 | 10^1 - 10^2 | Thickness of vessel | [31] |
| II. $\sigma_1 > \sigma_2 > \sigma_3 > 0$, true triaxial compression (TTC) | | | | | | |
| Servo-hydraulic confinement | Triaxial compression facility | Dolomite; Limestone | ~500 | $\sim 10^{-4}$ | Confinement effect; Failure criterion | [37] |
| | Drop-weight apparatus | Concrete | 2.5 | 10^0 - 10^1 | Confinement effect; Ultimate strength | [40] |
| | Servo-hydraulic triaxial system | Concrete | 16 | 10^{-5} - 10^{-3} | Confinement effect; Strain rate effect | [38] |
| | True triaxial testing machine | Granite | 250 | 10^{-5} - 10^{-4} | Energy evolution process | [39] |
| Coupling static-dynamic loading | 3D-Modified Hopkinson Bar | Concrete | ~50 | 10^1 - 10^2 | Dynamic stress; Fracture properties | [49] |
| | Triaxial Hopkinson Bar | Sandstone | 30 | 10^2 - 10^3 | Confinement effect; Fracture properties | [50] |
| | Triaxial Hopkinson Bar | Concrete | 60 | 10^1 - 10^3 | Strain rate effect; Strength criterion | [53] |
| | Triaxial Hopkinson Bar | Cement; Concrete | 30 | 10^2 - 10^3 | Stress-strain relationship | [52] |
| III. $\sigma_1 > \sigma_2 > \sigma_3 = 0$, biaxial compression (BC) | | | | | | |
| Tangential load | Biaxial strain rate machine | Granite | 501 | $\sim 10^{-1}$ | Stress-strain response; Strain rate effect | [41] |
| | Hydraulic biaxial system | Concrete | ~75 | 10^{-5} - 10^{-4} | Compressive strength; Stress-strain relationship | [42] |
| | Multiaxial testing system | Limestone | 20.7 | 10^{-5} - 10^{-4} | Strength behaviour | [43] |
| Servo-hydraulic confinement | Servo-hydraulic biaxial machine | Gypsum | 10 | 10^{-5} - 10^{-4} | Crack coalescence | [44] |
| | Servo-hydraulic multiaxial system | Concrete | 9 | 10^{-5} - 10^{-2} | Confinement effect; Strain rate effect | [45] |
| | Servo-hydraulic multiaxial system | Concrete | 35 | 10^{-5} - 10^{-2} | Influence of free water; dynamic strength; crack patterns | [5] |
| Biaxial dynamic compression | Biaxial split Hopkinson bar (SHB) | Concrete | ~50 | 10^2 - 10^3 | DIF; Fragmentation | [46] |
| | SHB with Hydraulic jack | Concrete | ~50 | 10^0 - 10^1 | Influence of initial stress | [47] |
| Coupling static-dynamic loading | Modified Kolsky bar | Ceramic | 400 | 10^2 - 10^3 | Fracturing process | [48] |
| | Triaxial Hopkinson Bar | Sandstone | 40 | 10^2 - 10^3 | Confinement effect; Fracture properties | [51] |

To explore the real-time fracturing process and post-failure crack patterns, non-contact measurement techniques e.g., DIC and micro-CT, have been widely used. The DIC method is popularly adopted in SHPB tests owing to its high accuracy, flexibility and easy operability [57-59]. 3D-DIC is realised by using the binocular stereovision principle [60-62], and has been successfully applied to 3D deformation measurements of geomaterials in conventional and triaxial SHPB tests [51, 63]. However, the real-time observation of fracturing processes and the measurement of heterogeneous deformation in concrete has not been fully studied. Thus, with the help of high-speed cameras and 3D-DIC, the heterogeneous deformation and fracturing process in concrete (e.g., strain fields around aggregates and developments of different crack types) under coupled static-dynamic loadings are

further explored. Moreover, micro-CT is powerfully used for reconstructing heterogeneous structures and microcracks of concrete with micron-level resolution [64-67]. Synchrotron-based micro-CT with high photon flux could significantly improve the image quality and realise characterisation of heterogeneous structures and different types of cracks [68]. However, there is still challenging in identification and classification of different crack types (e.g., matrix crack, interfacial crack and transgranular crack) in geomaterials based on traditional methods like manual extraction and automatic image segmentation. While manual extraction could recognise different types of cracks even in a low-quality image with much noise and low contrast, it is time-consuming and dependent on the subjectivity of visual inspection. Automatic image segmentation could deal with image data at a high speed, but it is very sensitive to the image quality and content [69, 70]. For example, noises, artifacts and pores in the image will disturb the segmentation process. Also, different types of cracks with the similar greyscale distribution can hardly be segmented. To overcome these shortcomings, machine learning as a promising method has been applied to image recognition in many fields, e.g., medicine, biology, chemistry, material science, geology and engineering [71-74]. It can extract user-defined image data based on training dataset with manual labelling, and reduce the disturbance caused by spurious image information [75, 76]. Therefore, a combination of synchrotron-based micro-CT and machine learning-based crack classification techniques is promising to achieve the recognition of different crack patterns with less time taken and greater accuracy, which will help understand the failure mechanisms of concrete.

This study aims to investigate the dynamic mechanical properties and fracturing behaviour of concrete under biaxial compressive loadings by using a Tri-HB system. Dynamic stress-strain curves considering confinement effect and strain rate effect are respectively analysed. Two high-speed cameras and a 3D-DIC technique are applied to capture the *in-situ* fracturing process and deformation fields. By using synchrotron-based micro-CT and machine learning-based crack classification techniques, internal fracture morphologies of post-failure specimens are reconstructed. Geometrical characteristics (e.g., orientation distribution, fractal dimension and position distribution) of different crack types are further analysed, and the effect of aggregate orientation and aspect ratio on crack types is considered. Additionally, the relationship among mechanical properties, fracture properties and fracture energy is also explored.

2. Experimental procedures

To study the dynamic mechanical properties and fracturing behaviour of concrete under biaxial confinements, ordinary concretes with basalt aggregates are adopted for these experiments. Non-contact measurement facilities including two high-speed cameras and synchrotron-based micro-CT, combined with 3D-DIC and machine learning-based crack classification techniques, are applied to capture the real-time deformation and fracturing process and analyse the post-failure fracture properties.

2.1 Specimen preparation

Concrete used in this study was mixed by water, cement, sand and aggregate in proportions of 0.6:1:2:3 by weight to achieve good workability (e.g., fluidity, cohesiveness and water retention) and the desired strength [77, 78]. Ordinary Portland cement (OPC), a general purpose cement produced in Australia, was used as the matrix. River sands with maximum size 1.12 mm and fineness modulus 1.86, and basalts with maximum size 7 mm were adopted as fine and coarse aggregates, according to ASTM C192 [79]. Basalt is used as coarse aggregate in this study owing to its higher density when compared with other common aggregates (e.g., limestone, granite, and other crushed rocks), which makes it easier to distinguish on the CT images.

The specimens were cast in steel moulds with dimensions of $54 \times 54 \times 54 \text{ mm}^3$ and covered with plastic film to prevent moisture loss owing to evaporation. 24 h later, they were demoulded and moist-cured in a special curing chamber at $23.0 \pm 2.0^\circ\text{C}$. After curing for 28 days, the specimens were ground to a size of 50 mm (presented in Fig. 2) and polished in accordance to the specification of ASTM C109 [80]. The quasi-static compressive properties were determined by a Shimadzu Autograph AGS-X compressive machine with a loading rate of 0.3 mm/min (strain rate 10^{-4} s^{-1}). The physical and mechanical properties are as follows: average density (ρ) = 2350 kg/m³, Young's modulus 3.8 GPa, uniaxial compressive strength (σ_c) = 45.0 MPa, P-wave velocity C_L = 4800 m/s, S-wave velocity C_S = 2750 m/s.

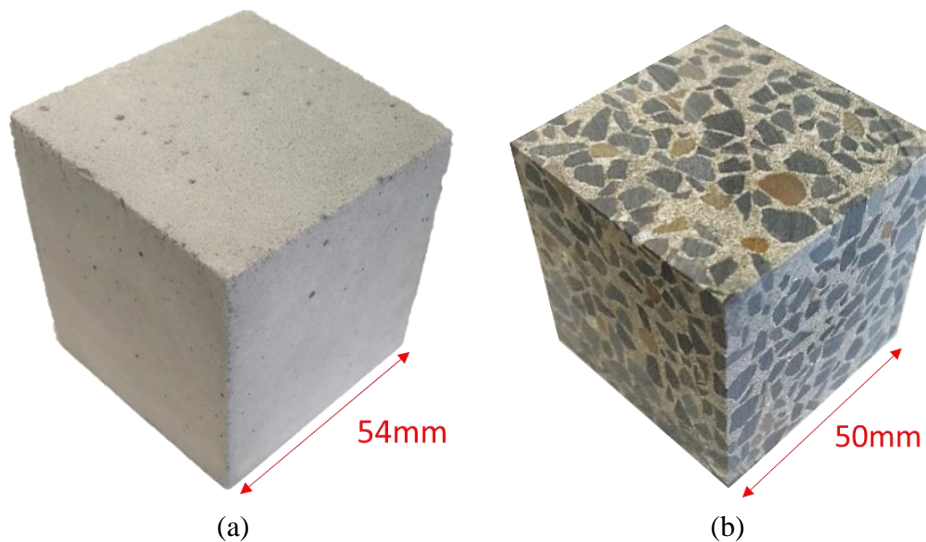


Fig. 2. (a) Casted concrete specimen and (b) prepared concrete specimen.

2.2 Dynamic biaxial compression testing

Dynamic tests of concrete specimens under biaxial confinements were carried out using a triaxial Hopkinson bar (Tri-HB) system, as shown in Fig. 3 (a). The system consists of a dynamic loading module and a confinement-loading module. The dynamic loading module includes a gas gun (1.5 m), a cylindrical striker (0.5 m), an incident bar (2.5 m) and a transmission bar (2 m). The confinement-loading module is composed of three

independent servo-controlled hydraulic cylinders (maximum pressure capacity 100 MPa), the incident and transmission bar in the X direction, four steel output bars (2 m) in the Y and Z directions, and six high-strength steel reaction frames installed on the strong supporting platform. The striker (diameter 40 mm) and bars (cross-section $50 \times 50 \text{ mm}^2$) are made of high-strength 42CrMo steel with following mechanical properties: density $\rho_b = 7850 \text{ kg/m}^3$, Young's modulus $E_b=210 \text{ GPa}$, longitudinal wave velocity $C_b = 5200 \text{ m/s}$ and yield strength $\sigma_Y = 930 \text{ MPa}$.

A schematic of a dynamic biaxial compression experiment with stereo camera set-up is shown in Fig. 3 (b). Firstly, the desired biaxial pre-stress conditions are applied by hydraulic cylinders in the X and Y directions. Then, dynamic loading along the X direction is generated by the striker impacting the incident bar with an expected velocity measured by a laser-beam based velocimeter (HPCSY-II). Meanwhile, two high-speed cameras (Phantom V2511) mounted on tripods on top of specimen are triggered simultaneously to capture the full-field deformation and fracture processes. To obtain the desired incident pulse characteristics, a copper disc (diameter 15 mm and thickness 1.5 mm) is used as a pulse-shaper to eliminate high-frequency oscillation components and control the rise time, so that the specimen can reach stress equilibrium before fracture occurs [81]. During the stress wave propagation along the steel bars, strain gauges (FLA-6-11) attached on the incident bar, transmission bar and output bars are used to record strain signals. These signals are transferred via a Wheatstone bridge arrangement and strain meter, and subsequently digitised to 12 bits by a data acquisition (DAQ) system (NI PXIe 5105) at a sample rate of 1 MHz.



(a)

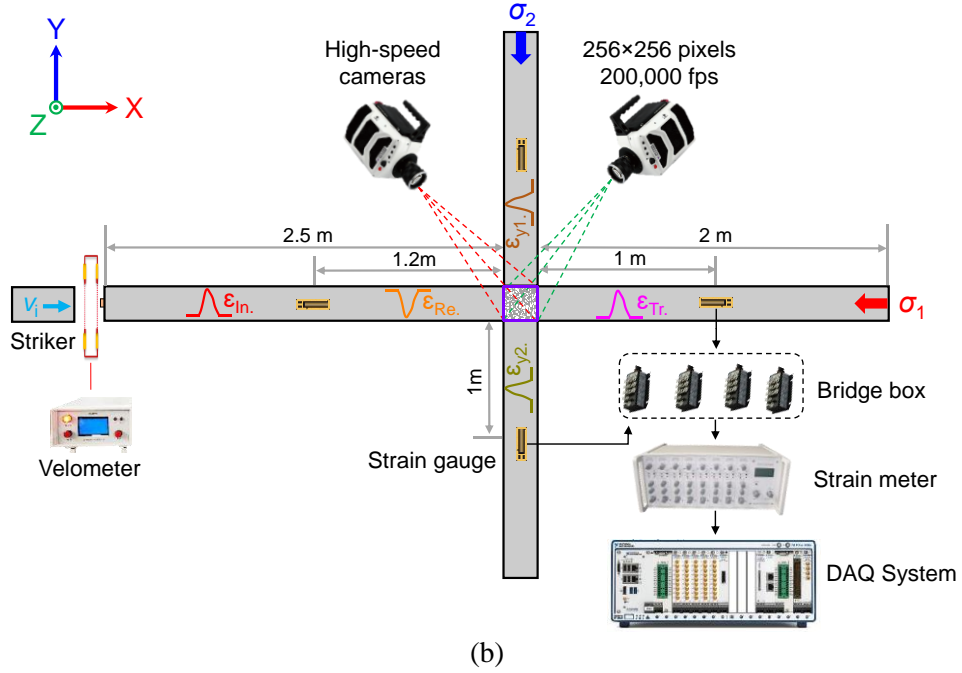


Fig. 3. (a) Triaxial Hopkinson bar (Tri-HB) system and (b) schematic of dynamic biaxial compression experiment (top view from the vertical Z direction).

The dynamic stress σ_d , strain rate $\dot{\varepsilon}$ and dynamic strain ε_d in each direction are calculated by elastic one-dimensional (1D) stress wave propagation theory using the following equations [50, 82]:

$$\sigma_x(t) = \frac{E_b A_b}{2A_s} [\varepsilon_{in}(t) + \varepsilon_{re}(t) + \varepsilon_{tr}(t)] = \frac{E_b A_b}{A_s} \varepsilon_{tr}(t) \quad (1)$$

$$\dot{\varepsilon}(t) = \frac{C_b}{L} [\varepsilon_{in}(t) - \varepsilon_{re}(t) - \varepsilon_{tr}(t)] = -\frac{2C_b}{L} \varepsilon_{re}(t) \quad (2)$$

$$\varepsilon(t) = \frac{C_b}{L} \int_0^T [\varepsilon_{in}(t) - \varepsilon_{re}(t) - \varepsilon_{tr}(t)] dt = -\frac{2C_b}{L} \int_0^T \varepsilon_{re}(t) dt \quad (3)$$

$$\sigma_y(t) = \frac{E_b A_b}{2A_s} [\varepsilon_{y1}(t) + \varepsilon_{y2}(t)] \quad (4)$$

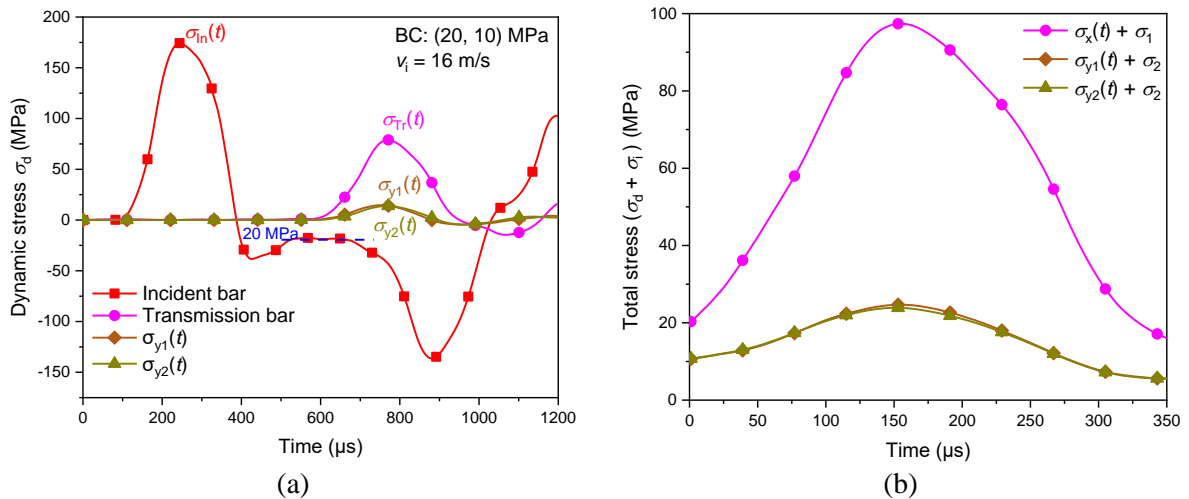
$$\varepsilon_y(t) = \frac{C_b}{L} \int_0^T [\varepsilon_{y1}(t) + \varepsilon_{y2}(t)] dt \quad (5)$$

where E_b , A_b and C_b are Young's modulus, cross-sectional area and the longitudinal wave velocity of the bars, respectively; A_s and L are the cross-sectional area and the length of the specimen; $\varepsilon_{in}(t)$, $\varepsilon_{re}(t)$ and $\varepsilon_{tr}(t)$ are the

incident, reflected and transmission strain signals measured by the strain gauges on the incident and transmission bars in the X direction; $\varepsilon_{y1}(t)$ and $\varepsilon_{y2}(t)$ are the strain signals on the two output bars in the Y direction induced by the Poisson's effect and specimen fracturing; $\sigma_x(t)$ and $\sigma_y(t)$ are the dynamic stresses along the X and Y direction; $\varepsilon_x(t)$ and $\varepsilon_y(t)$ are the dynamic strains along the X and Y directions; $\dot{\varepsilon}(t)$ is the strain rate.

Typical experimental results (including stress waves in the X and Y directions, total stress ($\sigma_d + \sigma_i$) evolution, stress equilibrium, and stress-strain curves) under pre-stress ($\sigma_1 = 20$, $\sigma_2 = 10$) MPa and impact velocity $v_i = 16$ m/s are shown in Fig. 4. Compression is defined as positive since all of the pre-stresses and impacts are compressive. The whole stress wave propagation along each bar is recorded in a period of 1200 μs as presented in Fig. 4 (a). It can be observed that a stress platform (approximately 20 MPa) follows the incident wave due to the loss of contact between the fixing device and incident bar during impact, indicating the applied axial pre-stress (i.e., 20 MPa) in the X direction. When the incident wave passes through the specimen, the specimen not only appears compressive deformation along the X direction, but also expands horizontally induced by the Poisson effect, inducing stress waves propagation along the Y direction as presented in Fig. 4 (b). The output bars in the Y direction experience stress waves with duration 400 μs and peak stress at 150 μs , consistent with the stress wave properties in the transmission bar, indicating that the Tri-HB system is able to capture the dynamic lateral confining effects.

The dynamic stress equilibrium is verified in Fig. 4 (c). The stress equilibrium between both ends of specimen lasts for over 100 μs before failure, i.e., over four wave reflections across the specimen. Under this circumstance, the inertial effect is reduced to a negligible level and the hypothesis of stress homogenisation along the specimen can be satisfied. Thus, based on 1D stress wave theory, the stress-strain histories of concrete specimen in X and Y directions can be calculated through Eqs. (1-5) and depicted in Fig. 4 (d).



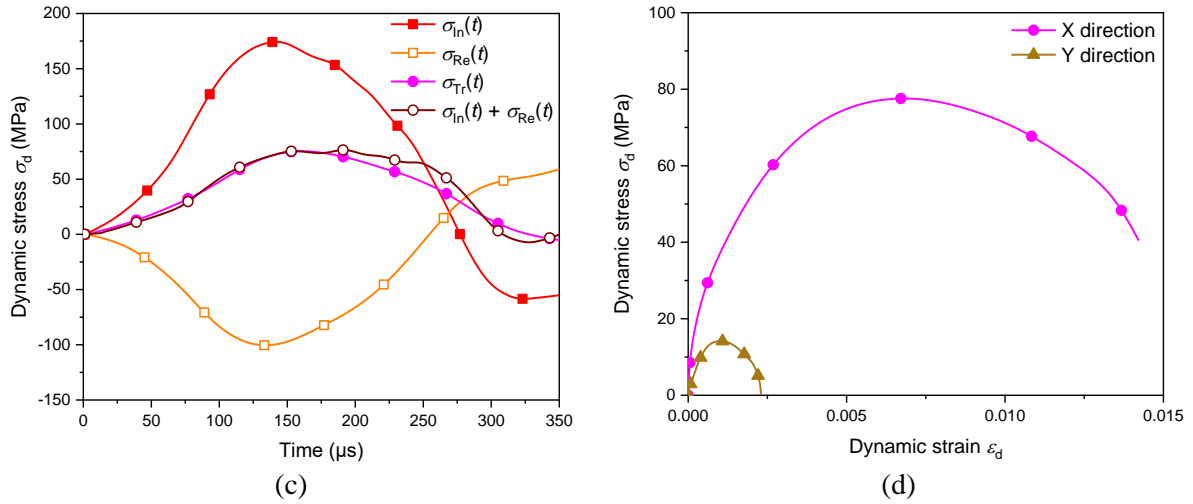


Fig. 4. Typical experimental results under biaxial compressive (BC) pre-stress (20, 10) MPa and impact velocity 16 m/s: (a) Stress waves in the X and Y directions; (b) total stress evolution in the X and Y directions; (c) dynamic stress equilibrium verification in impact direction and (d) dynamic stress-strain curves in the X and Y directions.

2.3 High speed 3D-DIC

The principle of 3D-DIC is based on the image registration of stochastic speckle patterns on specimen surface with two cameras in a stereoscopic configuration, as illustrated in Fig. 5. Firstly, the stereo calibration was carried out to get intrinsic and extrinsic parameters, e.g., focal length, principal point, lens distortion factor, scale coefficient, translation vector and rotation matrix. In order to obtain these calibration parameters, a calibration board ($100 \times 100 \text{ mm}^2$) was moved, rotated, and tilted on the specimen to get different calibration images. Two high-speed cameras were set to a resolution 1280×800 pixels, sampling rate 100 frames per second (fps) and exposure time $9900 \mu\text{s}$ so that the calibration board can be captured in a wide field of view. Then, the cameras were set to a resolution 256×256 pixels, sampling rate 200,000 fps and exposure time $4.5 \mu\text{s}$ to track the speckle patterns on the specimen surface under initiation and deformed states, and two 84W LED lights (GS Vitec MultiLED LT) were used for exposure compensation. Next, the initiation and deformed images of specimen were recorded by two high-speed cameras. By means of stereo correlation algorithm and calibration parameters, subset positions were transformed into 3D coordinates and the full-field spatial contours of the specimen surface under initiation and deformed states were depicted. Finally, displacement fields are calculated by subtraction of the spatial coordinates of the specimen surface under different states, and the strain fields and strain rate fields are obtained through the differentiation of displacement fields and strain fields.

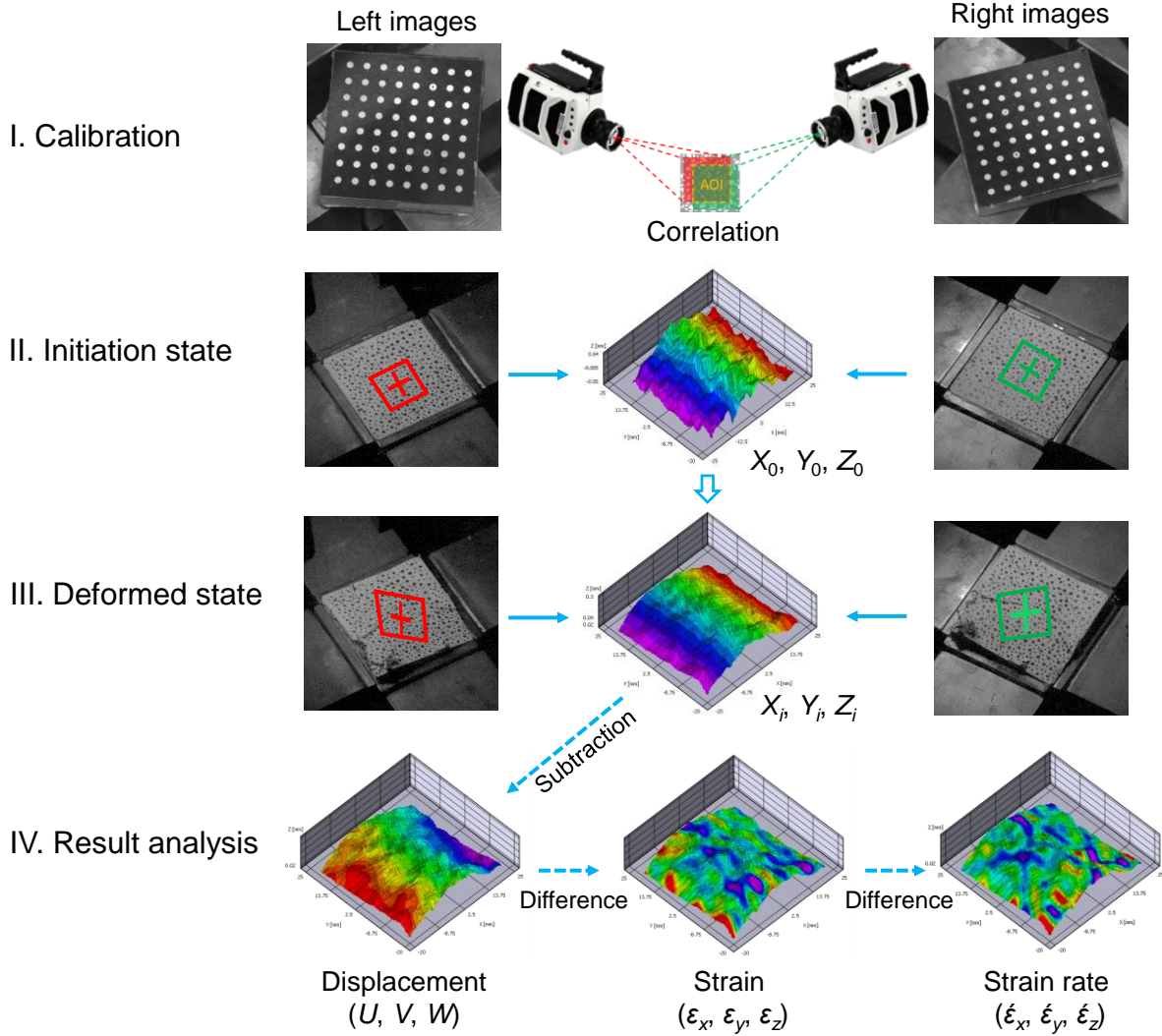


Fig. 5. Principle of 3D-digital image correlation (3D-DIC) technique.

2.4 Synchrotron-based micro-CT

The micro-CT technique at Australian Synchrotron Imaging and Medical Beam Line [83] was used to acquire data related to the internal structures and fractures of concrete. Fig. 6 shows the procedure of 3D fracture topology reconstruction (including CT scanning and CT image process). Before CT scanning, the post-test specimen was firstly placed on the rotation platform to conduct position calibration. Then, the CT scanning was carried out with the following setup parameters: X-ray energy 80 keV, specimen-detector distance 0.5 m, resolution 17.8 μm , rotation step 0.1°, exposure time 0.75 s and acquisition time 1.5 h. X-ray from the synchrotron beamline passed through the specimen and scintillator to the detector to generate 2D X-ray projections. After CT scanning, 2D greyscale slices, transformed from 2D X-ray projections, were imported into Avizo 9.5 software on the MASSIVE cluster. Owing to the differences in density and X-ray absorption capacity of concrete internal structures, aggregates, matrix, and cracks were distinguished clearly. Based on the different greyscale distributions between cracks and other materials, segmentation was carried out to extract the 2D fracture slices. Finally, 3D fracture topology was reconstructed by 3D rendering of 2D slices.

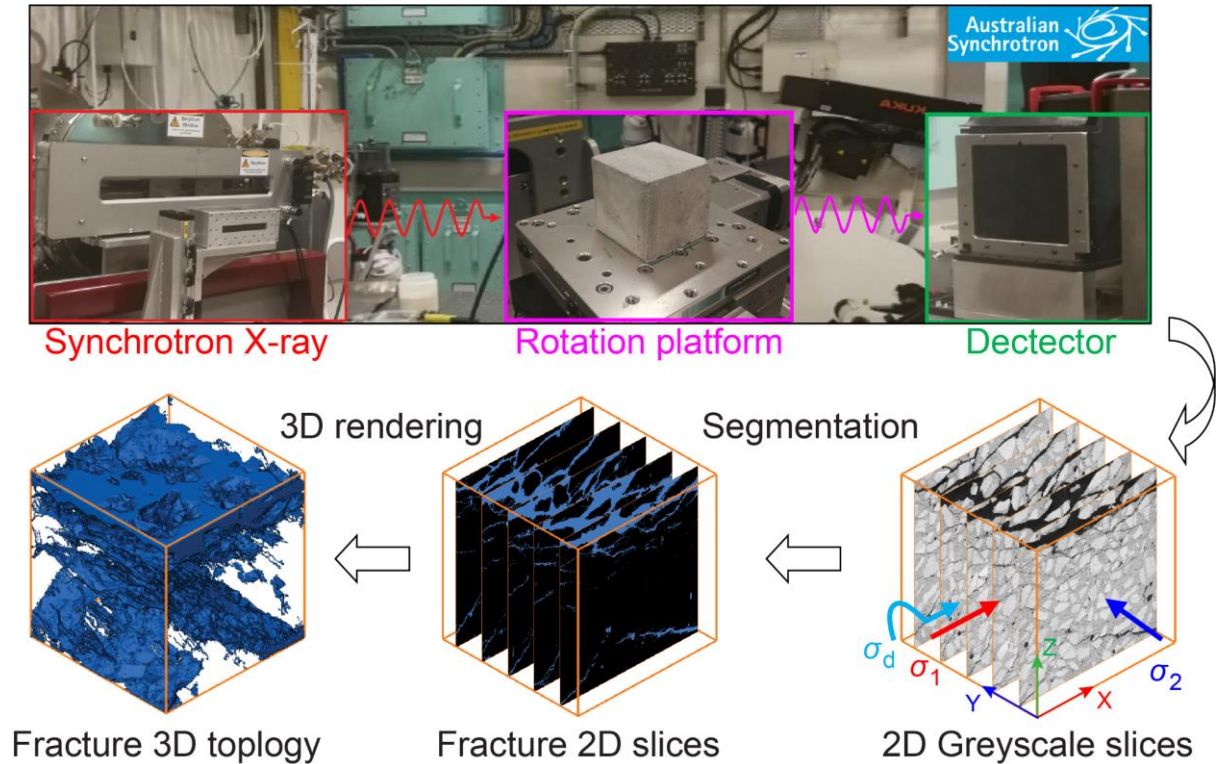


Fig. 6. 3D fracture topology reconstruction by synchrotron-based micro-CT.

2.5 Machine learning-based crack classification

The machine learning method adopted in this study is the trainable weka segmentation (TWS) project, which combines the image processing software Fiji [84] with the machine learning algorithms provided in the Waikato Environment for Knowledge Analysis (WEKA) software [85]. It can employ user-defined image features to train classifiers and provide unsupervised segmentation processes. In recent years, TWS has been successfully adopted to recognise structures of cells and tissues in biological science [86, 87]. However, it has not been applied to the research of concrete-like materials.

To extract and analyse different crack patterns in concrete specimens, the procedure of machine learning-based crack classification and microcrack statistic is as follows (Fig. 7): (1) CT image selection: at least 35 slices (3-5 representative concrete CT slices for each case) were loaded into TWS project as training sets; (2) crack classification: matrix cracks, interfacial cracks and transgranular cracks in training sets were labelled individually to train three corresponding classifiers, and then CT images to be analysed (at least 100 slices for each case) were loaded into the TWS project with three different classifiers to produce three individual image sets with different crack types; (3) geometrical statistics: lengths and orientations of different types of cracks in 2D greyscale slices were calculated by ImageJ for further statistical analysis.

As displayed in Fig. 7, matrix cracks, interfacial cracks and transgranular cracks are extracted individually and well matched with the different types of cracks in the original image data. Disturbances like noise and pores are also removed in the classified images, which implies that TWS is an efficient tool to extract user-defined image

features with minimal disturbance of other information in the image data. It should be mentioned microcracks (less than 1mm in length) in classified images (especially in image of interfacial cracks) will be filtered before statistical analysis. After the geometrical statistics of different cracks, their geometrical characteristics like orientation distribution, fractal dimension and position distribution are further analysed.

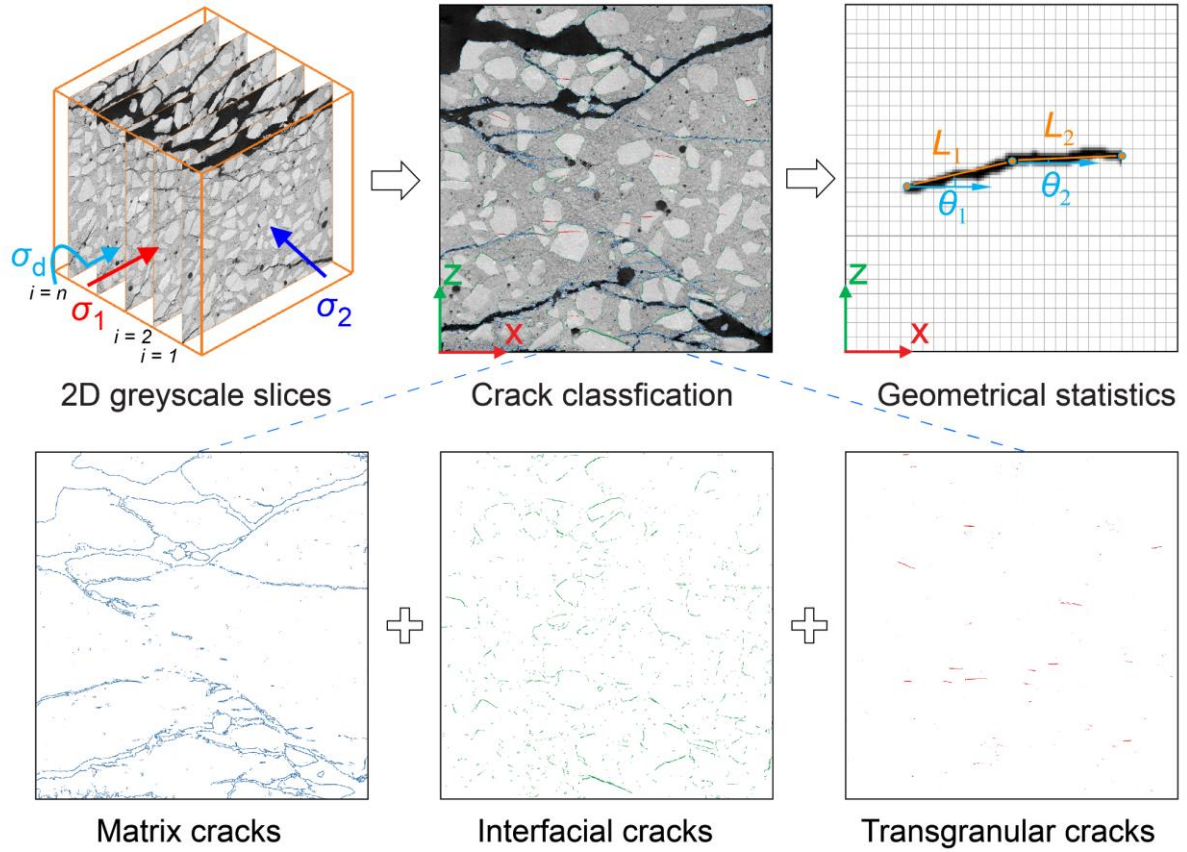


Fig. 7. Topological statistics of different types of cracks (blue: matrix crack; green: interfacial crack; red: transgranular crack)

To represent the complexity of cracks, fractal dimension is an effective factor [88-90]. In this study, box counting dimension D_0 (one classical fractal dimension factor) is used as follows:

$$D_0 = \lim_{b \rightarrow 0} \frac{\frac{1}{n} \sum_{i=1}^n \ln(N_i)}{\ln(1/b)} \quad (6)$$

where n is the total number of X-Z slices taken into analysis and N_i is the box count of slice i under box size b .

Average crack density $\rho(z)$ (average crack length in unit area along the Z direction) is adopted to describe the position distribution properties with the following equation.

$$\rho(z) = \frac{1}{n} \sum_{i=1}^{i=n} \frac{l_i(z)}{\Delta S_i} \quad (7)$$

where $l_i(z)$ is the crack length in cell area with unit length along the Z direction in slice i , and ΔS_i is the cell area divided along the Z direction.

Areas of different crack types $A_{f,matrix}$, $A_{f,inter}$, and $A_{f,trans}$, and total crack areas A_f are respectively calculated by following equations.

$$A_{f,matrix} = \Delta d \sum_{i=1}^{i=n} l_{i,matrix} \quad (8)$$

$$A_{f,inter} = \Delta d \sum_{i=1}^{i=n} l_{i,inter} \quad (9)$$

$$A_{f,trans} = \Delta d \sum_{i=1}^{i=n} l_{i,trans} \quad (10)$$

$$A_f = A_{f,matrix} + A_{f,inter} + A_{f,trans} \quad (11)$$

where Δd is the interval distance of each slice, $l_{i,matrix}$, $l_{i,inter}$, and $l_{i,trans}$ are length of matrix cracks, interfacial cracks and transgranular cracks in slice i .

In addition, from the observation of the image data, it is found that aggregates with different geometrical properties generate different types of cracks. In order to explore the effect of aggregate geometrical properties on the crack types, aggregates with interfacial cracks and transgranular cracks are extracted by the following steps (Fig. 8): (1) at least 100 CT slices for each case were selected to take the analysis; (2) aggregates in 2D greyscale slices of post-failure concrete are extracted by threshold; (3) pre-processing routines such as ‘‘dilate’’ and ‘‘fill-holes’’ are executed to restore the aggregates to an approximate initial state without cracks; (4) pre-processed aggregates are labelled individually and their position coordinates are extracted; (5) the coordinates of interfacial cracks and transgranular cracks obtained by TWS are also extracted and mapped to the positions of labelled aggregates; (6) labelled aggregates with interfacial cracks or transgranular cracks are respectively extracted by judging the relative position of cracks and aggregates; (7) original aggregates in 2D greyscale slices are extracted by superposition with pre-processed aggregates; (8) the aggregate geometrical characteristics (e.g., orientation, major axis and minor axis) are collected by aggregate ovalisation; and (9) batch process is executed

to replicate the steps above and the final geometrical statistics (e.g. aspect ratio and orientation) of aggregates with interfacial and transgranular cracks were summarised and analysed.

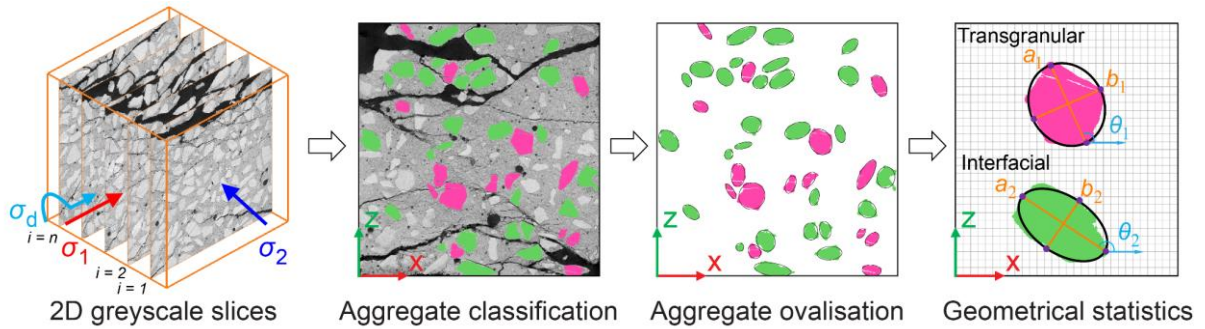


Fig. 8. Topological statistics of aggregates with interfacial and transgranular cracks.

3. Dynamic mechanical properties and fracturing evolution

The dynamic stress-strain curves and real-time deformation and fracturing process of concrete under different biaxial confinements (i.e., pre-stress σ_1 and σ_2 varied from 5 to 30 MPa) and impact velocities (i.e., 14, 16 and 18 m/s) are respectively explored. There are at least 3 specimens tested for each loading condition to minimise the influence of differences in the specimens and experimental errors.

3.1 Effect of confinement

The effect of confinements on dynamic stress-strain curves of concrete is shown in Fig. 9, with the same impact velocity of 16 m/s but under different biaxial compressive pre-stresses.

Generally, the dynamic strength decreases with increasing axial pre-stress σ_1 along the impact direction, but increases with lateral pre-stresses σ_2 . The variation of the peak strain (namely the strain at the peak stress) under different pre-stresses is similar to that of peak stress. Pre-existing microcracks are reactivated by pre-stress σ_1 along the impact direction and thus facilitating the failure process during impact, While lateral confinement σ_2 suppresses the crack growth and restricts the lateral deformation, resulting in an increase of dynamic strength [91, 92]. Stress-strain curves under various pre-stresses have different post-peak features. For example, with the increase of pre-stress σ_1 , the stress strain curve shows obvious ductility after the peak stress. When pre-stress σ_2 is increased, the stress strain curve exhibits a rebound phenomenon in the post-peak state; this is because the specimen still retains a certain amount of elastic energy.

For stress-strain curves in the Y direction, the changes are contrary to the results in the X direction. Peak stress and peak strain in the Y direction are improved with an increase of pre-stress σ_1 , but decreased with an increase of pre-stress σ_2 . The reason for this observation is lateral deformation during dynamic loading is promoted with axial pre-stress but restricted by lateral confinements. The influence of pre-stress σ_2 on peak stress and peak

strain in the Y direction is more obvious than σ_1 , indicating that lateral confinements could more effectively restrict lateral deformation along the Y direction.

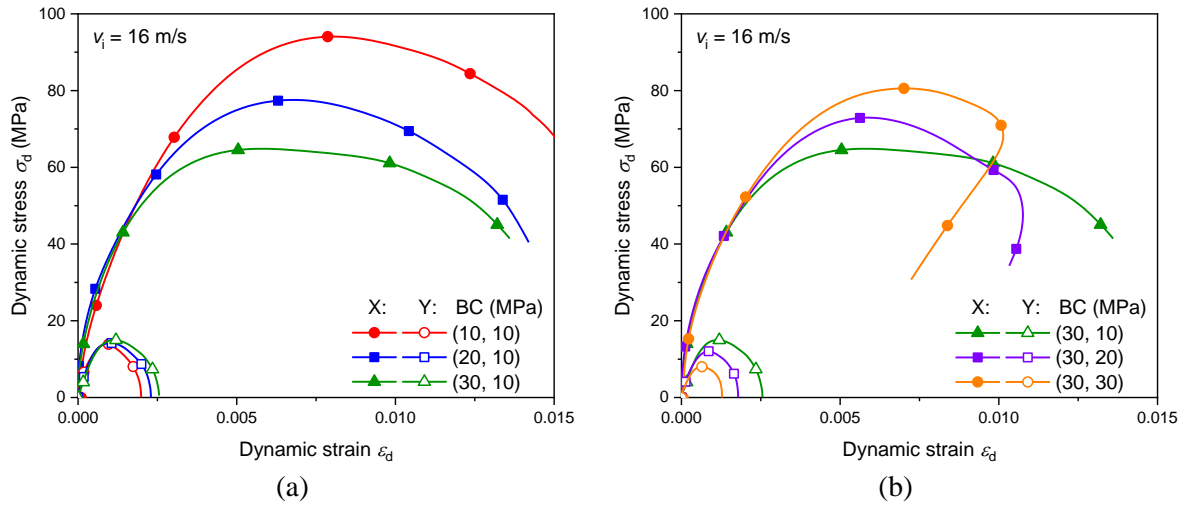


Fig. 9. Effect of biaxial compressive (BC) pre-stress of varied (a) σ_1 and (b) σ_2 on dynamic stress-strain curves of concrete under impact velocity $v_i = 16$ m/s.

3.2 Effect of strain rate

In order to explore the strain rate effect of concrete under biaxial pre-stress conditions, biaxial pre-stress states of (5, 5), (10, 5) and (20, 5) MPa were examined under different impact velocities (e.g., 14, 16 and 18 m/s), corresponding to approximate strain rates of 80, 110, and 140 s^{-1} respectively. The loading conditions are carefully designed so that the fracture properties of post-test specimens can be further analysed by CT scanning, which is introduced in section 4.1. The typical dynamic stress-strain curves of concrete in X and Y directions under different impact velocities and biaxial pre-stress are shown in Fig. 10. Both of the peak stress and peak strain in the X and Y directions are rate-dependent. Under the pre-stress of (5, 5) MPa, an obvious strain recovery in the post-peak stage is observed at impact velocities of 14 and 16 m/s but disappears under a higher impact velocity of 18 m/s. A similar observation is obtained under the pre-stress of (10, 5) MPa with increasing impact velocity. Under the pre-stress of (20, 5) MPa, the stress-strain curves exhibit obvious ductile deformation at the post-peak stage, indicating that the increase of the stress deviator aggravates the development of shear cracks under dynamic loading.

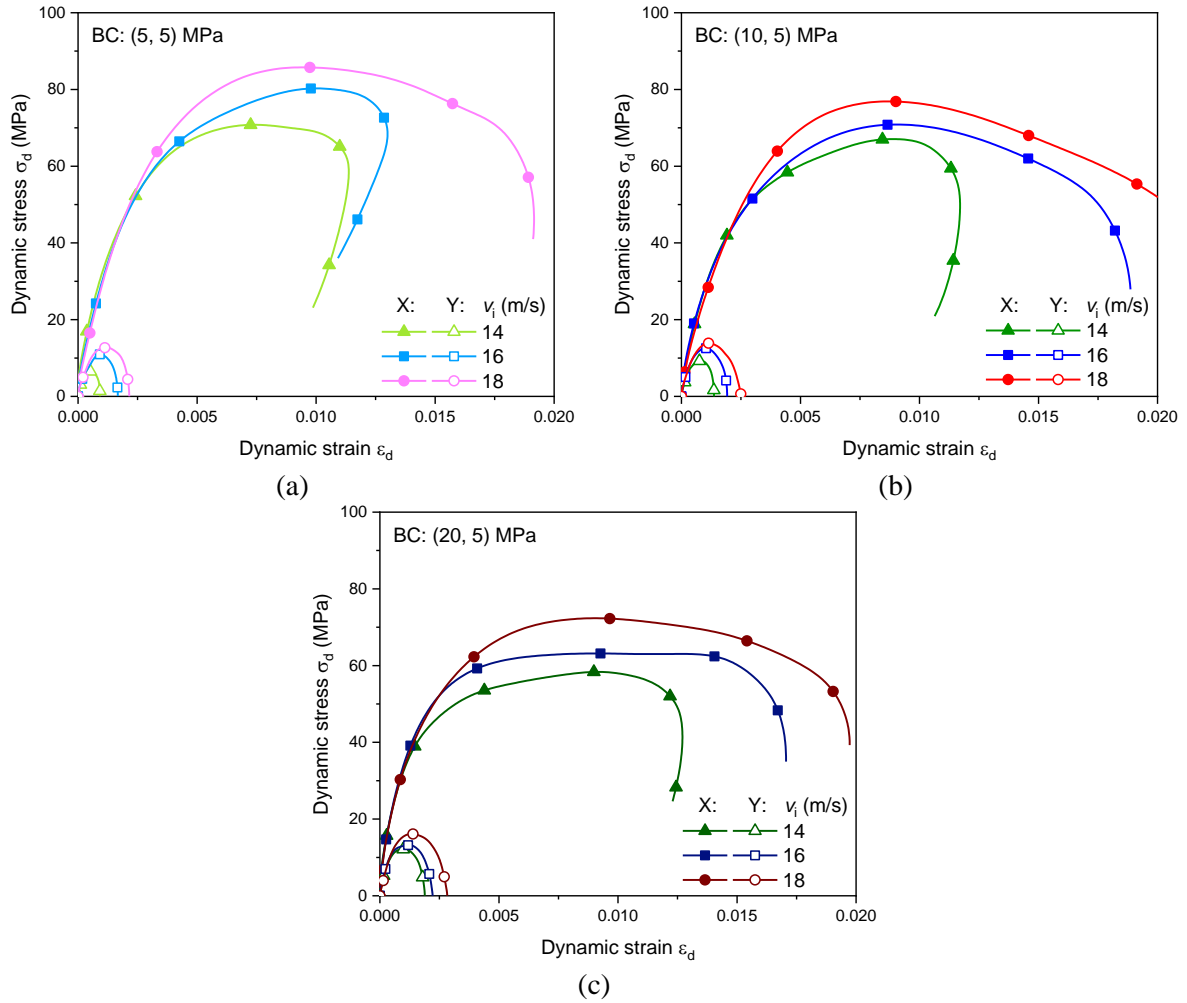


Fig. 10. Effect of impact velocity on dynamic stress-strain curves of concrete under biaxial pre-stresses of (a) (5, 5) MPa, (b) (10, 5) MPa, and (c) (20, 5) MPa.

Under different biaxial confinements (pre-stress $\sigma_1 \geq \sigma_2$, $\sigma_2 = 5, 10$ and 20 MPa) and different impact velocities ($v_i = 14, 16$ and 18 m/s), the effect of strain rate $\dot{\epsilon}$ on total stress ($\sigma_d + \sigma_1$) under different lateral pre-stresses σ_2 is summarised in Fig. 11. The results not only show the rate effect, but also present the influence of lateral confinement on the rate effect, i.e., the trend of strength enhancement with strain rate becomes pronounced when lateral confinement increases from 5 to 20 MPa. These results clearly show the effect of intermediate principal stress σ_2 , and could be considered for the calibration of dynamic constitutive models of concrete.

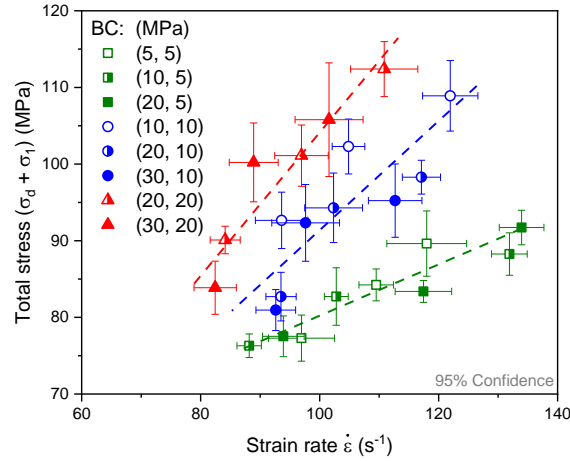


Fig. 11. Effect of strain rate on total stress ($\sigma_d + \sigma_1$) of concrete under different biaxial pre-stresses.

3.3 Full-field deformation and fracturing process

The deformation and fracturing processes of geomaterials under dynamic loadings are affected by their heterogeneity. Fig. 12 shows a typical real-time fracturing process of concrete under an impact velocity of 16 m/s and a pre-stress of (20, 10) MPa. The stress strain curve is marked with representative time stamps and displayed in Fig. 12 (a). The surface fracture evolution captured by the high-speed cameras is shown in Fig. 12 (b). In the first 50 μ s, there is no obvious crack on the surface, which is consistent with the elastic stage in the stress-strain curve shown in Fig. 12 (a). Then at 100 μ s, interfacial cracks and matrix cracks appear near the incident and transmission edges. When the peak stress is reached at around 150 μ s, cracks propagate from the edges to the middle of the specimen surface along the impact direction. After the peak stress, transgranular cracks appear at around 200 μ s with matrix and interfacial cracks further developed.

The full-field strain map calculated by 3D-DIC technique is shown in Fig. 12 (c). In the axial strain fields (e_{xx}) at 100 μ s, tensile strain localisation appears near the incident edge, which corresponds to the interfacial cracks observed in Fig. 12 (b). Compressive strain localisation areas are also observed, relevant to the inhomogeneous deformation around aggregates due to the differences in elastic modulus. In the lateral strain (e_{yy}) fields at 100 μ s, tensile strain localisation along the impact direction appears, indicating the initiation of main cracks with the same propagation direction. Then at 150 μ s, lateral tensile strain localisation propagates along the loading direction, in accordance with the propagation direction of matrix cracks in Fig. 12 (b). Tensile strain localisation also appears in the compressive strain localisation area observed in the axial strain fields (e_{xx}) at 100 μ s, indicating that the inhomogeneous deformation around the boundary of aggregates is likely to be a weak zone for easier crack propagation. In the post-peak stage at 200 μ s, lateral tensile strain localisation further develops along the impact direction. In addition, it is noticed that lateral tensile strains are asymmetric at pre-peak stage, which is mainly induced by heterogeneous distribution and irregular shapes of aggregates near surface. In order to explore the effect of aggregate on crack properties, the relationship between aggregate geometrical properties and crack patterns is further studied in Section 4.3.

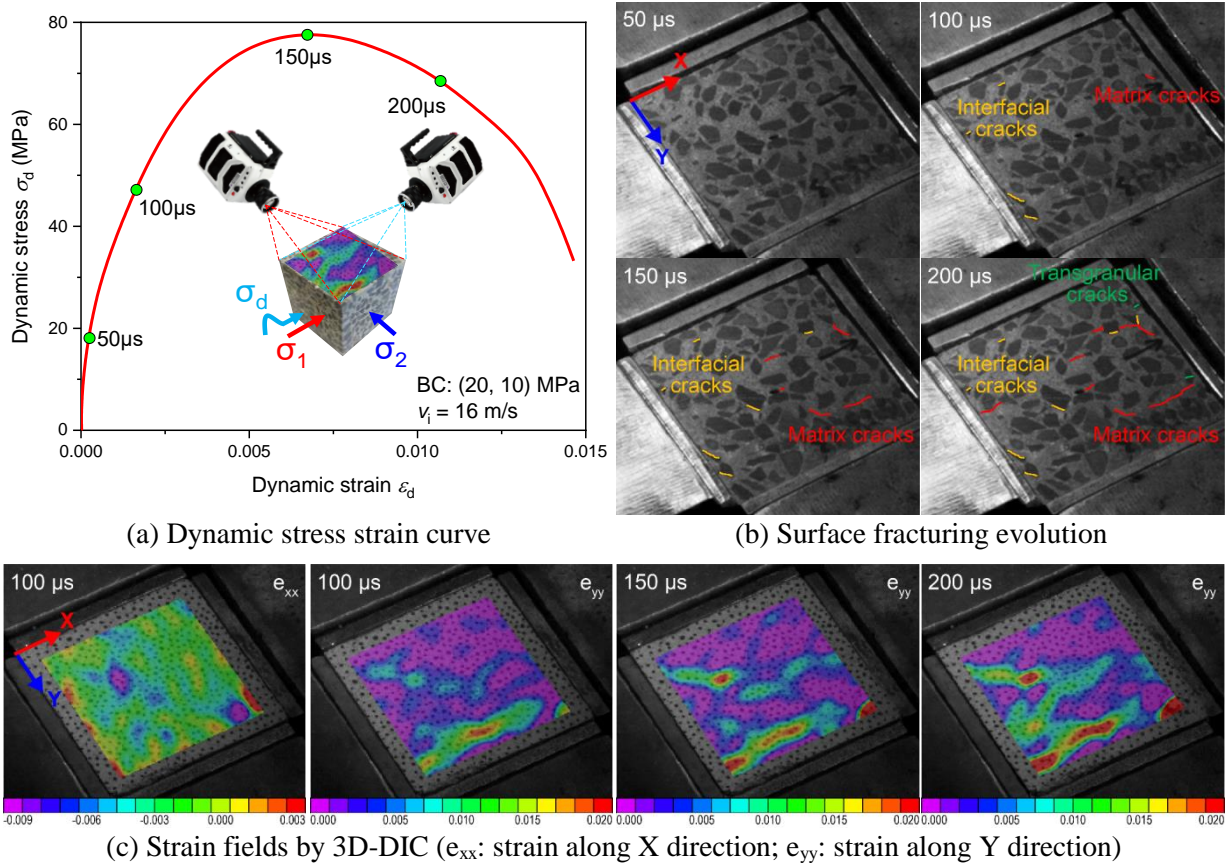


Fig. 12. Fracture evolution of concrete under pre-stress (20, 10) MPa and impact velocity $v_i = 16$ m/s ($\dot{\epsilon} \approx 100$ s⁻¹).

Typical high-speed photographs of concrete failure process under different biaxial pre-stresses of (10, 10), (30, 10), (30, 20) and (10, 5) MPa and impact velocities of 14, 16 and 18 m/s are summarised in Fig. 13. It shows that failure process of concrete is transformed from local damage near the incident end to slab ejection towards the transmitted end with the increase of pre-stress σ_1 , while it is changed from slab ejection to local fracture near the transmitted end when pre-stress σ_2 increases. This phenomenon indicates the aggravation effect of axial pre-stress σ_1 and the restriction effect of lateral confinement σ_2 on the failure process, as is also shown by stress-strain curves. The effect of impact velocity is also prominent since there is no obvious crack on the surface at an impact velocity of 14 m/s but visible cracks can be observed at higher impact velocities (e.g., 16 and 18 m/s).

| v_i (m/s) | BC | High-speed photography of concrete failure process | | | | |
|----------------|----------|--|-----------------------|-----------------------|------------------------|------------------------|
| | | $t = 50 \mu\text{s}$ | $t = 250 \mu\text{s}$ | $t = 500 \mu\text{s}$ | $t = 1000 \mu\text{s}$ | $t = 2000 \mu\text{s}$ |
| 16 | (10, 10) | | | | | |

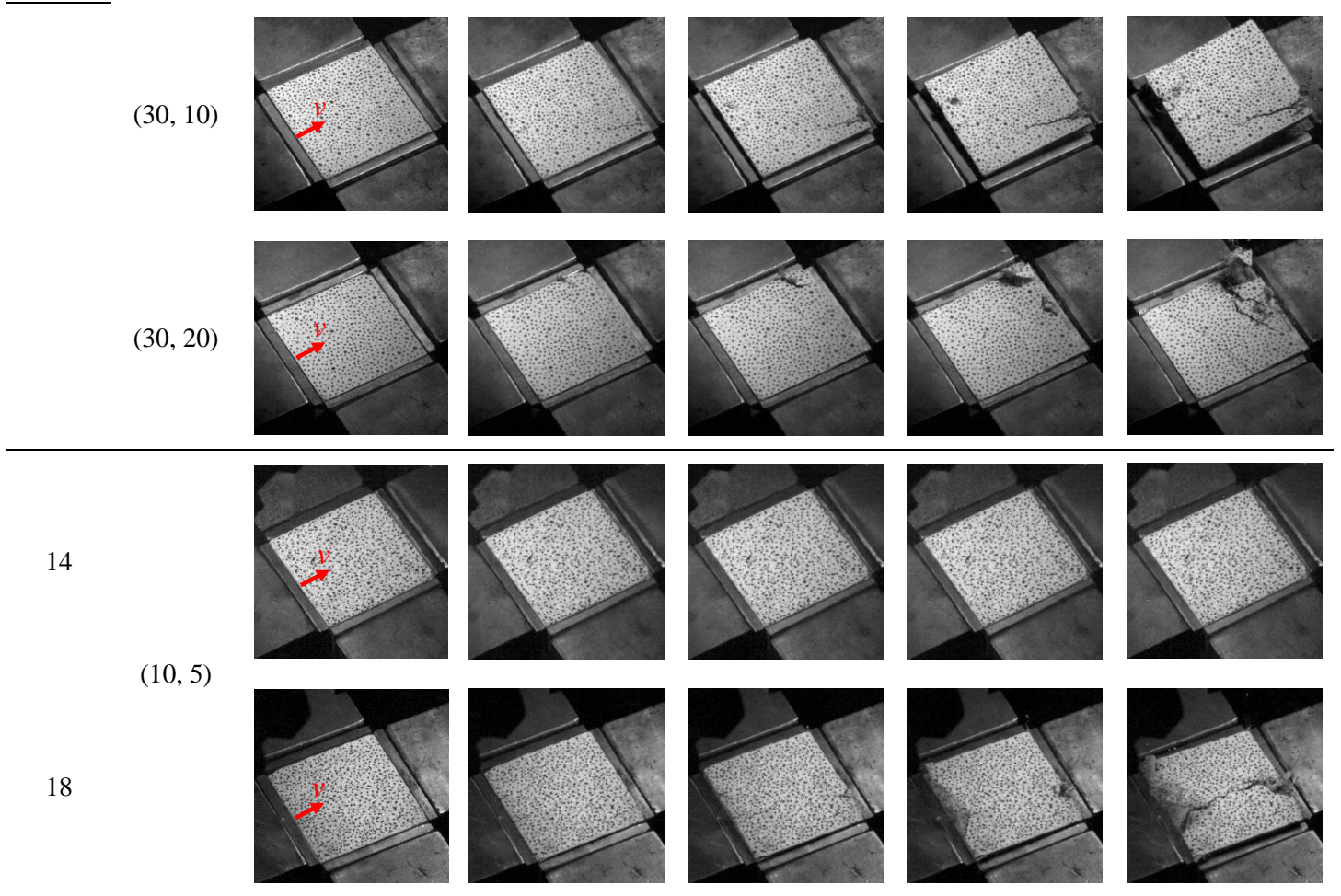
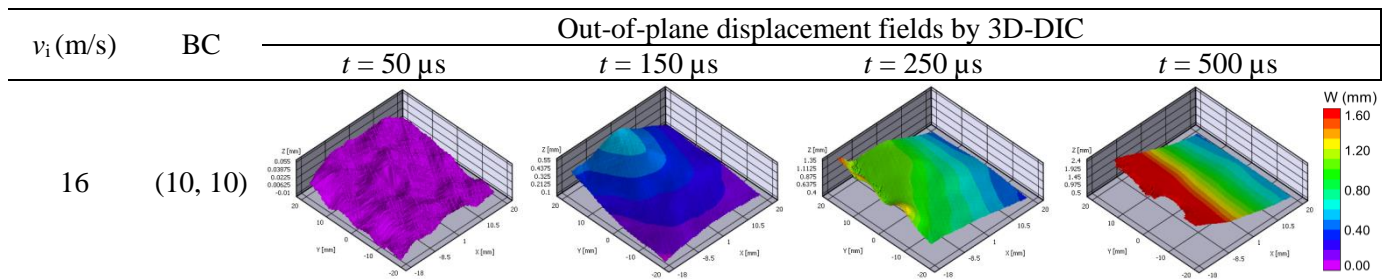


Fig. 13. Failure process of concrete under coupled static and dynamic loadings.

The corresponding real-time full-field deformation captured by 3D-DIC is summarised in Fig. 14. Generally, during the first 150 μs , the specimen exhibits a bending deformation with larger expansion at the middle part along the impact direction due to the friction between the specimen and bars. After 250 μs , the maximum deformation is shifted from the middle part to the incident or transmitted end of the specimen, forming an upwarp deformation. Meanwhile, as the augment of impact velocity, the surface deformation pattern is changed from bending dilation at an impact velocity of 14 m/s to upwarp deformation at higher impact velocities (e.g., 16 and 18 m/s).



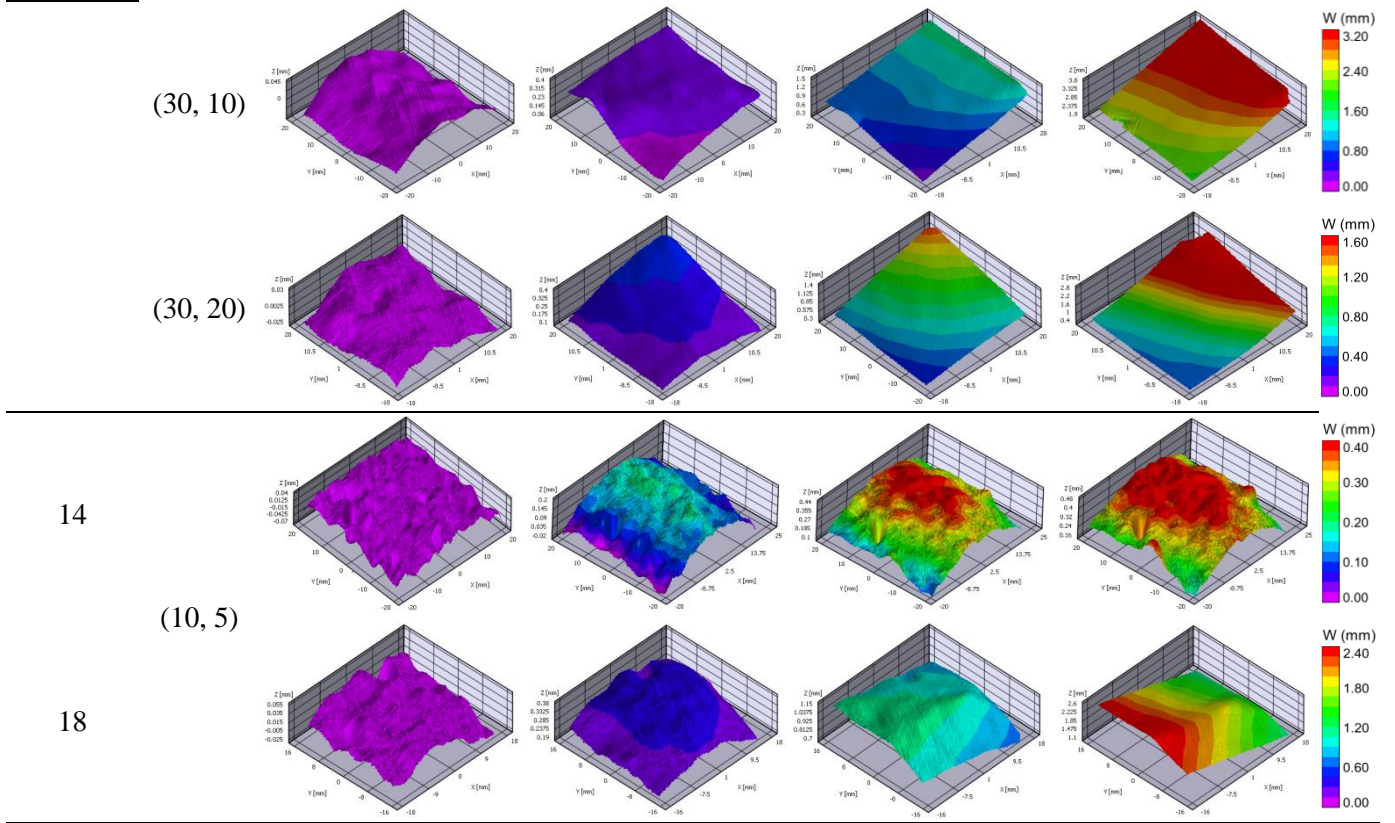


Fig. 14. Out-of-plane displacement fields of concrete under coupled static and dynamic loadings.

Fig. 15 shows that the out-of-plane displacement of specimen increases with pre-stress σ_1 and impact velocity but decreases with pre-stress σ_2 . More specifically, out-of-plane displacement presents linear growth with time under the pre-stresses σ_2 of 10 MPa, but transforms into decelerated increase under higher pre-stresses σ_2 of 20 and 30 MPa. Meanwhile, the pre-stress σ_2 has a more prominent effect on the variation of peak displacement than pre-stress σ_1 as illustrated in Fig. 15 (a). In addition, the impact velocity also has obvious influence on the evolution of out-of-plane displacements as shown in Fig. 15 (b). During the first 250 μ s, out-of-plane displacement increases under different impact velocities. During 250~500 μ s, it keeps stable at an impact velocity of 14 m/s, transforms into decelerated increase at an impact velocity of 16 m/s and appears near-linear growth at an impact velocity of 18 m/s. By comparing Fig. 15 (a) and Fig. 15 (b), it can be found that the out-of-plane displacement at 500 μ s increases from 1.93 mm to 3.79 mm when the confinement changes from (30, 30) MPa to (30, 10) MPa, while the corresponding value under (20, 5) MPa increases from 0.47 mm to 3.71 mm when the impact velocity increases from 14 m/s to 18 m/s. The result indicates that impact velocity has more prominent influence on the out-of-plane displacement compared with confinement.

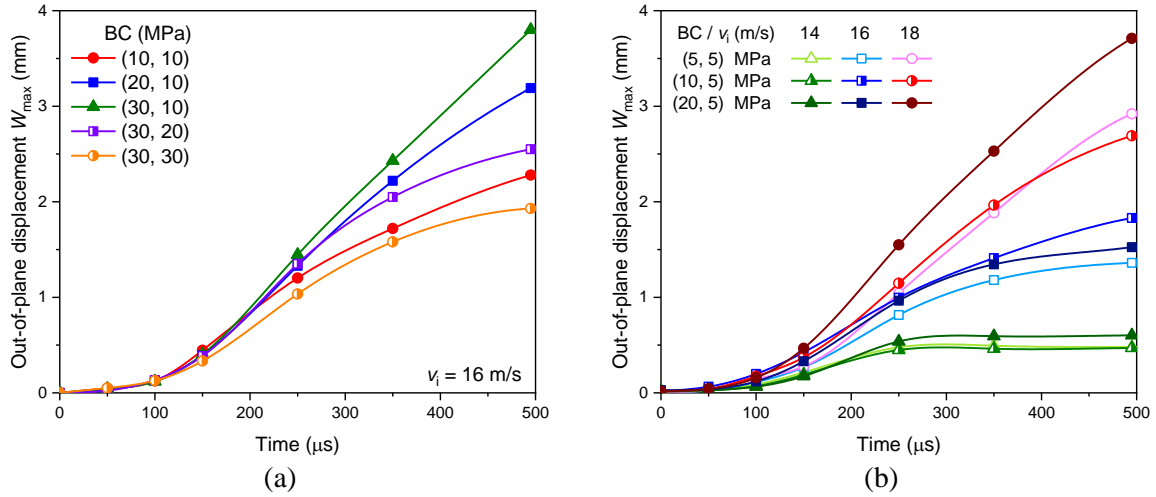


Fig. 15. Evolution of maximum out-of-plane displacement W_{max} under (a) different pre-stresses and (b) impact velocities.

4. Post-failure fracture characteristics

Dynamic stress-strain results and real-time deformation and fracturing process mainly reflect the mechanical and fracturing properties of concrete at the macro- and meso-levels. In order to have a deeper understanding of the failure mechanism, the post-failure fractures and different crack patterns are further studied at the micro-level by means of synchrotron-based micro-CT and machine learning-based crack classification techniques in this section.

4.1 Post-failure fractures

2D X-Z slices, 3D fracture topology and fracture volume V_f under different confinements and impact velocities are summarised in Fig. 16 and Fig. 17, respectively. Generally, fractures mainly concentrate on the top and bottom parts of each specimen since deformation develops towards free faces.

From Fig. 16 it is clearly observed that the fracturing zone is aggravated with axial pre-stress σ_1 but restrained by lateral confinement σ_2 , since microcracks are reactivated by axial pre-stress σ_1 and restrained by lateral confinement σ_2 . Apart from the fractures appearing at the top and bottom of specimens, shear bands can also be observed in the middle part of specimens under deviator stress conditions (i.e., pre-stress σ_1 not equal to σ_2) from 2D X-Z slices. This implies that the stress deviator along two principal stress directions induces the activation of shear cracks and thus promotes the formation of shear bands, which is further validated from the stress-strain curve in Fig. 9 (a) and Fig. 10 (c). Compared with 2D crack slices, 3D fracture topology depicts the fractures in a stereoscopic perspective. It shows that cracks evolve from the surface to the interior and side to the middle of the specimen as pre-stress σ_1 increases, consistent with the crack propagation process observed in Fig. 12. When pre-stress σ_2 increases, the fracturing zone decreases and cracks can be hardly observed in the middle part of the specimen from the 3D fracture topology. Additionally, as verified from out-of-plane displacement in Fig. 15, pre-stress σ_2 has more prominent effect on the fracture volume variation than pre-stress σ_1 .

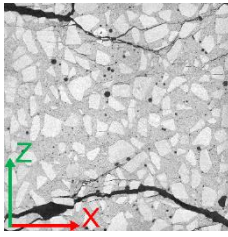
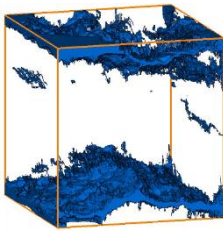
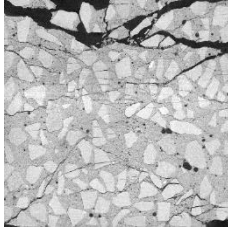
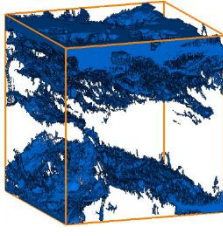
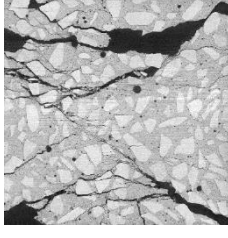
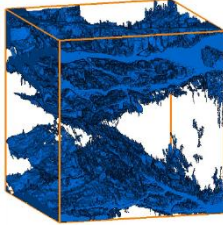
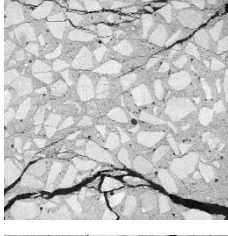
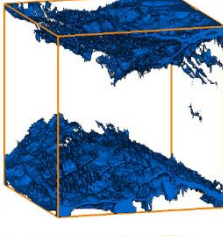
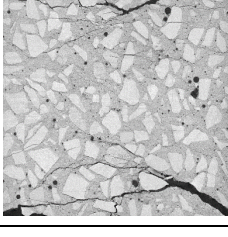
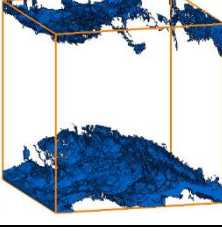
| (σ_1, σ_2) MPa | 2D X-Z slices | 3D fracture topology | V_f (mm ³) |
|-------------------------------|---|--|--------------------------|
| (10, 10) |  |  | 6864 |
| (20, 10) |  |  | 11398 |
| (30, 10) |  |  | 16623 |
| (30, 20) |  |  | 8269 |
| (30, 30) |  |  | 4412 |

Fig. 16. Post failure fractures of concrete under different pre-stresses with impact velocity 16 m/s.

From Fig. 17, it can be seen that the level of fracturing is significantly increased with impact velocity. More specifically, cracks are more likely to initiate and propagate along the interface at an impact velocity of 14 m/s and coalesce in the matrix at higher impact velocities (e.g., 16 and 18 m/s). Meanwhile, more transgranular cracks are observed with increasing impact velocity from the 2D slices [93]. Cracks mainly initiate at the top and bottom parts of the specimen and also appear in the middle part near the incident edge at an impact velocity of 14 m/s. At higher impact velocities (e.g., 16 and 18 m/s), cracks at the top and bottom get further developed and shear bands gradually coalesce in the centre part of specimen. In addition to the fracture volume quantified by 3D fracture topology, different crack types (e.g., matrix cracks, interfacial cracks and transgranular cracks)

are further explored in the following section for better understanding of the failure patterns and failure mechanism.

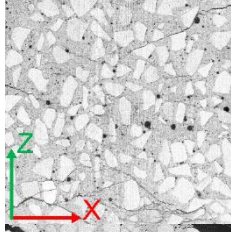
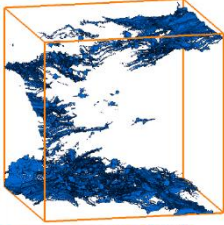
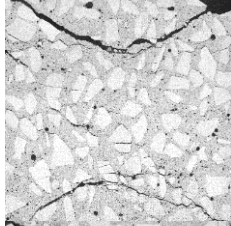
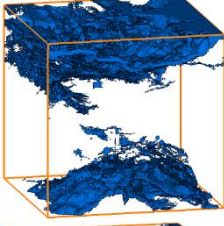
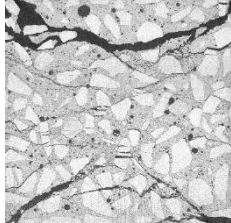
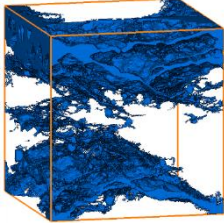
| v_i (m/s) | 2D X-Z slices | 3D fracture topology | V_f (mm ³) |
|----------------|--|---|-----------------------------|
| 14 |  |  | 1471 |
| 16 |  |  | 7142 |
| 18 |  |  | 14845 |

Fig. 17. Post failure fractures of concrete with pre-stress (10, 5) MPa under different impact velocities.

4.2 Geometrical characteristics of crack patterns

To achieve statistics relating to the different crack types, X-Z slices are mainly considered since cracks mainly propagate in the X-Z plane (i.e., plane of the maximum and minimum principal stresses). By applying the TWS method mentioned before, different crack patterns (e.g., matrix cracks, interfacial cracks and transgranular cracks) are well labelled and extracted. By further analysis of their geometrical characteristics, the crack orientations under different biaxial pre-stresses are displayed with the wind rose diagram. Fig. 18 shows typical results of orientation distribution of different cracks under pre-stress (20, 10) MPa with impact velocity $v_i = 16$ m/s. Orientations of matrix cracks are mainly located in the range of 0-40 and 140-180 degrees from the impact direction, which is in line with the main fracture properties observed in the 3D volume rendering. Interfacial cracks show disperse distribution, as orientations of interfacial cracks are not only affected by the directions of main cracks but also by the random interface directions around aggregates. Contrary to the interfacial crack distribution, the orientations of transgranular cracks are so uniform that almost most of the transgranular cracks are parallel to the impact direction within the range of 20 degrees, which implies that transgranular cracks are mainly induced by tensile stress along Z direction towards the free surface. For better visualisation of crack orientation information, it can be referred to the CT images in Fig. 16.

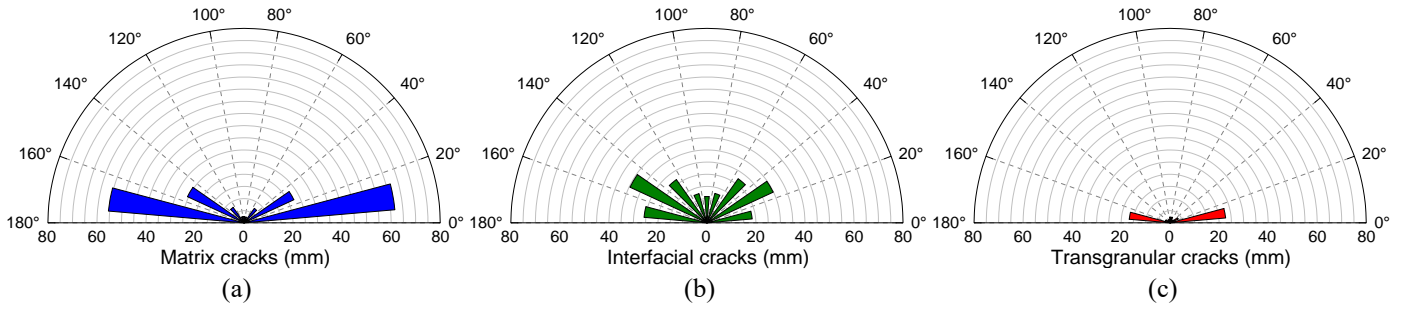


Fig. 18. Typical results of orientation distribution of different cracks under pre-stress (20, 10) MPa with impact velocity $v_i = 16$ m/s ($\dot{\epsilon} \approx 100$ s⁻¹).

Apart from the crack orientation distributions, the fractal dimension and position distribution along the Z direction of different crack types. From Fig. 19 (a) it can be seen that the fractal dimensions of different crack types are distinct. Matrix cracks have the highest values, indicating that matrix cracks have more complicated geometrical characteristics, for example more microcracks, intersected cracks, and coarse crack boundaries. Interfacial cracks have slightly fewer fractal dimensions compared with matrix cracks, and their difference gets decreased with larger box size. Compared with matrix and interfacial cracks, the fractal dimension of transgranular cracks are relatively much lower, indicating that transgranular cracks not only have uniform orientations, but also have similarly regular geometrical properties, e.g., smoother boundaries and linear shapes. The geometrical characteristics of the three crack types can also be observed in Fig. 7.

Fig. 19 (b) shows the position distribution of different crack types under pre-stress (30, 20) MPa. Overall, different crack types have obviously varying position distribution properties. Position distributions of matrix cracks, consistent with the fracture distributions observed in the 3D volume rendering as summarised in Fig. 16, are mainly located in the top and bottom parts of specimen (a range of 15 mm distance from the surface) but rarely located in the middle part. Interfacial cracks also have similar distributions as matrix cracks, but with less variation. The proportion of interfacial cracks is relatively higher in the middle part of the specimen compared to the other two crack types. It is interesting to notice that the position distributions of transgranular cracks are totally different to those of the matrix cracks and the interfacial cracks. The transgranular cracks are mainly concentrated in the middle part of specimen. Combined with the other transgranular geometrical characteristics, some reasons are speculated as follows. Firstly, the difference in elastic modulus between the matrix and aggregates induces compressive strain concentration around aggregates in the XY plane, which is verified by DIC results shown in Fig. 12 (c). Meanwhile, the centre parts of specimens suffer higher confinements due to the effect of inertia [94]. Accordingly, aggregates under high biaxial confining pressure will have more deformation towards the two free surfaces, resulting in tensile stress along Z direction and generation of tensile cracks, which can be verified by the orientation distribution and fractal dimension properties of transgranular cracks shown in Fig. 18 and Fig. 19 (a). Secondly, during dynamic loading, the propagation stress wave experiences diffraction and pressure retro-reflection around aggregates. Due to the stress shielding effect of aggregates, the compressive stresses at the fore-and-aft faces of aggregates along the impact direction are imbalanced, producing a bending effect towards the impact direction and inducing transgranular cracks which

can be observed in the CT slices shown in Fig. 16. The bending effect theory has been reported in previous research on the response of reactor pressure vessels to detonation waves, conducted by the United States Atomic Energy Commission [95].

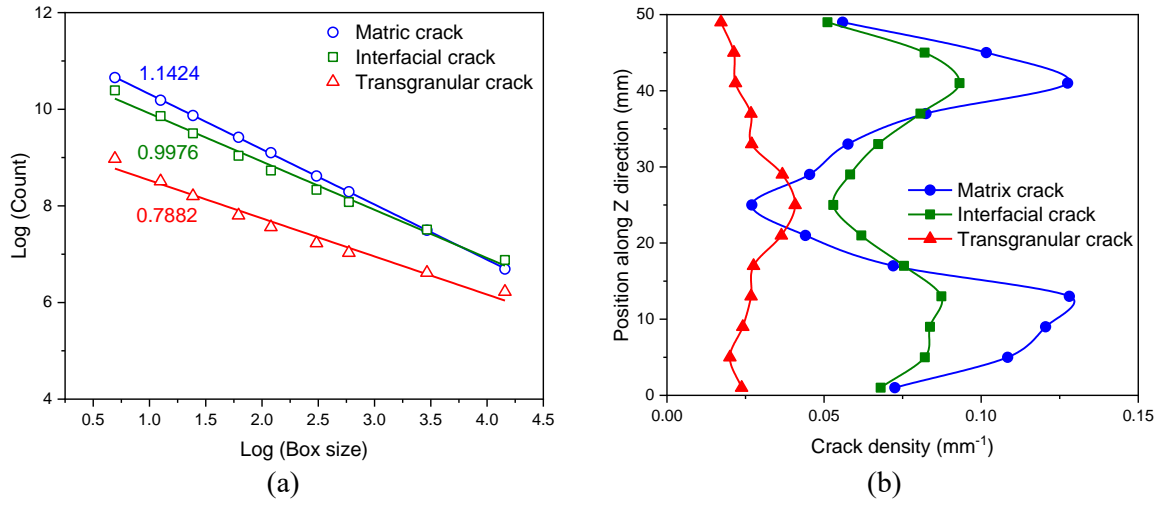


Fig. 19. Typical results of (a) fractal dimensions and (b) position distribution of crack density along Z direction of different types of cracks under pre-stress (30, 20) MPa with impact velocity $v_i = 16$ m/s ($\dot{\epsilon} \approx 90$ s⁻¹).

4.3 Effect of aggregate on crack patterns

By statistical analysis of the aggregate geometrical properties (e.g., orientation and aspect ratio), the effect of aggregates on crack patterns is clarified and shown in Fig. 20. Generally, transgranular cracks are more likely to appear in aggregates whose orientation is perpendicular to the impact direction (orientation among 60-120 degrees), but interfacial cracks are more likely to propagate across aggregates whose orientations more closely align with the loading direction (orientation among 0-60 and 120-180 degrees). Meanwhile, the aspect ratio of aggregates will increase the orientation effect on crack types, i.e., aggregates with high aspect ratios are more likely to generate transgranular cracks when their orientations are perpendicular to the impact direction, but more likely to form interfacial cracks when their orientations are parallel. Furthermore, it can also be seen from Fig. 20 that vertical elongated aggregates are more likely to form transgranular cracks along the impact direction, consistent with the geometrical characteristics of transgranular cracks. Thus, it can be concluded that aggregate orientation and aspect ratio have an effect on crack types.

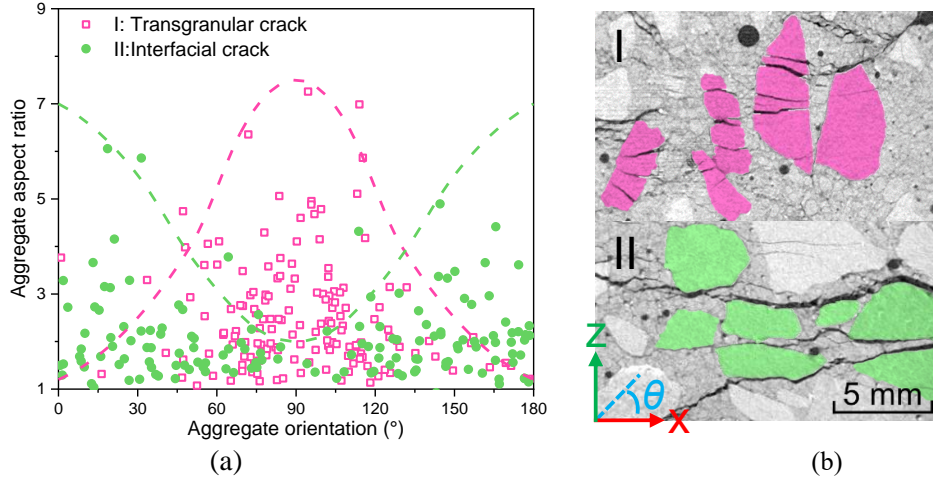


Fig. 20. (a) Geometrical distributions of aggregates with (b) transgranular and interfacial cracks under pre-stress (20, 10) MPa with impact velocity $v_i = 16$ m/s ($\dot{\epsilon} \approx 100$ s⁻¹).

4.4 Dynamic fracture energy analysis

Fracture energy is an important parameter for geomaterials under high strain rates, and is correlated to the mechanical properties and fracture behaviour [21]. In order to explore the relationship among fracture properties, mechanical properties and fracture energy, areas of different crack types and total cracks are respectively calculated with Eqs. (8-11), and energy absorbed by the testing specimen under pre-stresses and dynamic loadings is calculated as follows [51]:

$$W_s = W_0 + W_{in} - W_{re} - W_{tr} - W_{y1} - W_{y2} \quad (12)$$

where W_s is the energy absorbed by concrete specimen; W_0 is strain energy stored in the specimens during the biaxial pre-stresses; W_{in} , W_{re} , and W_{tr} are the energies carried by the incident, reflected, transmitted waves along the X direction; W_{y1} and W_{y2} are the output strain energies along the Y direction. They are calculated by following equations [96]:

$$W_0 = \frac{m}{2\rho} \sum \frac{\sigma_i^2}{E_i} \quad (13)$$

$$W_{in} = \frac{A_b C_b}{E_b} \int \sigma_{in}(t)^2 dt \quad (14)$$

$$W_{re} = \frac{A_b C_b}{E_b} \int \sigma_{re}(t)^2 dt \quad (15)$$

$$W_{tr} = \frac{A_b C_b}{E_b} \int \sigma_{tr}(t)^2 dt \quad (16)$$

$$W_{y1} = \frac{A_b C_b}{E_b} \int \sigma_{y1}(t)^2 dt \quad (17)$$

$$W_{y2} = \frac{A_b C_b}{E_b} \int \sigma_{y2}(t)^2 dt \quad (18)$$

where m and ρ are the mass and density of the concrete specimens; σ_i and E_i are the principal pre-stresses and corresponding elastic modulus; $\sigma_{in}(t)$, $\sigma_{re}(t)$, and $\sigma_{tr}(t)$ are dynamic stresses from the incident, reflected, transmitted waves along the X direction; $\sigma_{y1}(t)$ and $\sigma_{y2}(t)$ are dynamic stresses along the Y direction, respectively.

Assuming that the absorbed energy is totally directed to fracturing and the kinetic energy of ejection is neglected considering its limited effect, the fracture energy G_f is calculated as follows:

$$G_f = \frac{W_s}{A_f} \quad (19)$$

where A_f is the total area of fractures, which is introduced in details in section 2.4.

As can be seen in Fig. 21 (a) and (b), the areas of different crack types are basically in accordance with the variation of fracture volume, i.e., decreasing with pre-stress σ_1 , and increasing with pre-stress σ_2 and impact velocity. The area of interfacial cracks is generally higher than matrix cracks under pre-stress (10, 10) MPa and impact velocities of 14 and 16 m/s, but lower than matrix cracks under other loading conditions. Compared with matrix cracks and interfacial cracks, transgranular cracks have much lower areas and are more affected by impact velocity than pre-stress. When taking absorbed energy into account, it is found that absorbed energy is significantly increased with impact velocity, which is consistent with the variation in crack areas. However, absorbed energy under different pre-stress conditions shows a different trend to that of crack areas. Absorbed energy is slightly increased with pre-stress σ_1 but apparently improved when pre-stress σ_2 increases from 10 to 20 MPa.

The transgranular crack ratio, total stress and fracture energy of concrete under different pre-stress and impact velocities are presented in Fig. 21 (c) and (d). All of them decrease with pre-stress σ_1 but increase with pre-stress σ_2 and impact velocity. Compared with the impact velocity, pre-stress has a more significant effect on fracture energy. Besides, it can be seen that when the transgranular crack ratio increases, the total stress and fracture energy both increase, indicating that the transgranular crack plays an important role in determining the mechanical properties and fracture energy. At the same time, the positive correlation between total stress and

fracture energy is also consistent with the relationship between strength and fracture toughness in previous studies [97-99].

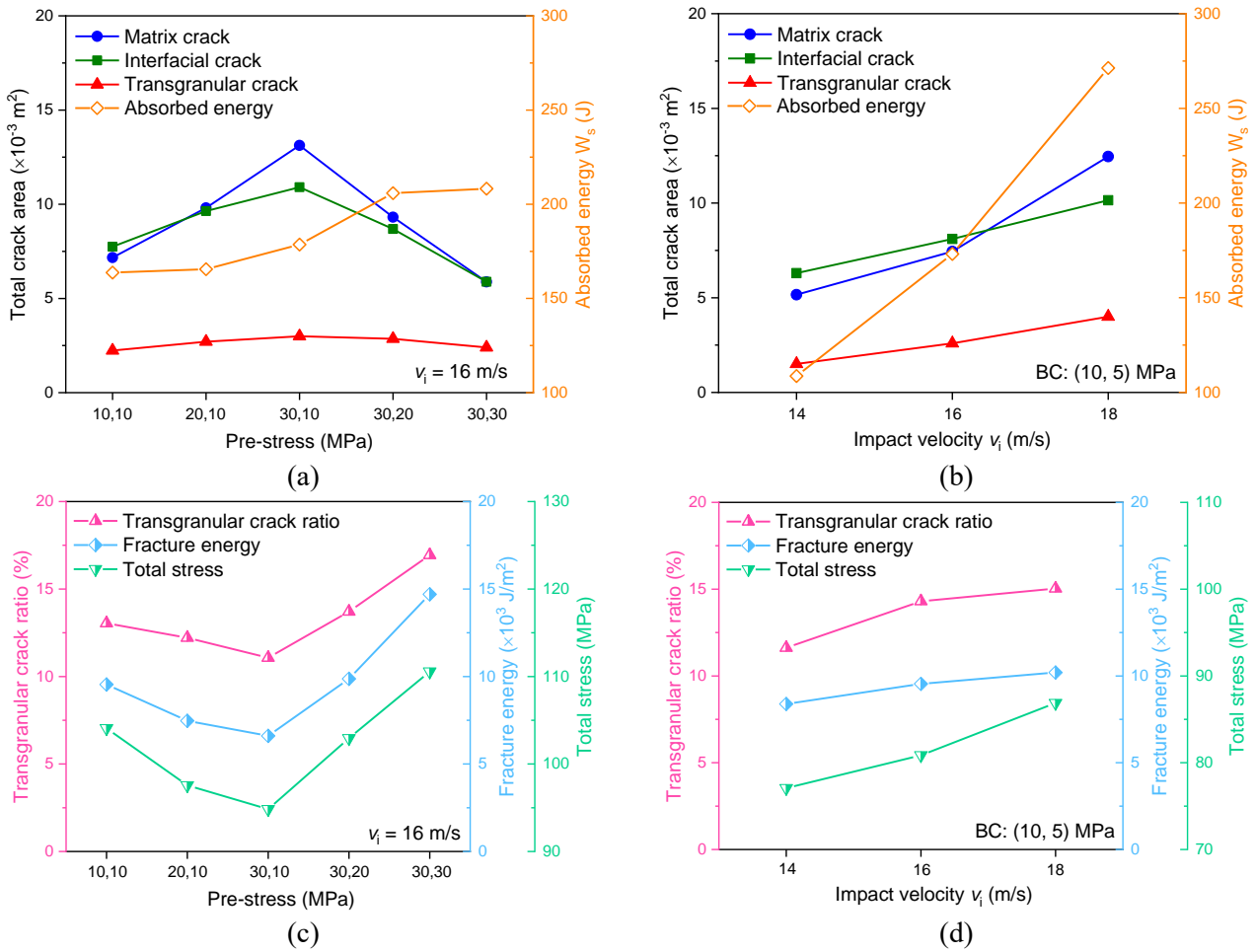


Fig. 21. Areas of different crack types and absorbed energy under (a) different pre-stresses and (b) different impact velocities, relationship among transgranular crack ratio, total stress and fracture energy under (c) different pre-stresses and (d) different impact velocities.

5. Conclusions

The dynamic mechanical properties and fracture behaviour of heterogeneous geomaterials (taking concrete as an exemplar) under biaxial confinements are studied for the design and safety managements of civil infrastructures and mining activities. In this study, by utilising a triaxial Hopkinson bar system, high-speed cameras combined with 3D-DIC, synchrotron-based micro-CT and machine learning-based image processing techniques, the dynamic stress-strain relationship, real-time deformation and fracturing evolution process, as well as the post-failure fracture properties are explored. The main conclusions are as follows:

- (1) The dynamic strength and peak strain of concrete show a clear strain rate effect and confinement effect, i.e., decreasing with axial pre-stress σ_1 , and increasing with lateral pre-stress σ_2 and impact velocity. However, peak stress and peak strain in lateral directions show the opposite effect. Additionally, stress-strain curves have different post-peak responses which are dependent on the confinement conditions.

- (2) The real-time deformation and fracturing results show that cracks generally propagate from the sides to the middle of specimens along the impact direction, appearing at interfaces and in the matrix first and in aggregates afterwards. Meanwhile, compressive strain concentrations are observed around aggregates demonstrating the effect of heterogeneity. In addition, the level of surface fracturing and out-of-plane displacement increases with pre-stress σ_1 and impact velocity but decreases with pre-stress σ_2 , which is consistent with the post-failure fracture volume.
- (3) Machine learning based image processing and geometrical crack statistics show that different crack types have distinct geometrical characteristics, i.e., orientation distribution, fractal dimension and position distribution. Additionally, the orientation and aspect ratio of aggregates have an obvious influence on the transgranular cracks and interfacial cracks, i.e., aggregates with larger aspect ratio and orientation (60° - 90°) are more likely to generate transgranular cracks, but elongated aggregates parallel to impact direction tend to generate interfacial cracks.
- (4) The areas of three different crack types and the absorbed energy have similar growth tendency with pre-stress σ_1 and impact velocity, but higher energy is consumed with lower fracture area under higher lateral confinements due to the prominent increase of fracture energy. Transgranular crack ratio, total stress and fracture energy are correlated under different pre-stresses and impact velocities, indicating the importance of transgranular cracks in the mechanical properties and fracture energy of concrete under dynamic loading.

Acknowledgements

This work was financially supported by the Australian Research Council (LE150100058, IH150100006 and DE200101293). The first author would like to acknowledge the Monash-China Scholarship Council (CSC) Scholarship (201807090100), and thank Dr. Lie Kong of Monash University for discussion on crack characteristics. The specimens were scanned in the Imaging and Medical beamline (IMBL) at the Australian Synchrotron (Project M14709), and special thanks to Dr. Chris Hall, Dr. Anto Maksimenko and Dr. Daniel Hausermann at Australian Synchrotron for their kind supports.

Reference

- [1] E. Brunesi, R. Nascimbene, Extreme response of reinforced concrete buildings through fiber force-based finite element analysis, *Engineering Structures* 69 (2014) 206-215, <https://doi.org/10.1016/j.engstruct.2014.03.020>
- [2] J.C. Gill, B.D. Malamud, Reviewing and visualizing the interactions of natural hazards, *Reviews of Geophysics* 52(4) (2014) 680-722, <https://doi.org/10.1002/2013rg000445>
- [3] F. Gutiérrez, M. Parise, J. De Waele, H. Jourde, A review on natural and human-induced geohazards and impacts in karst, *Earth-Science Reviews* 138 (2014) 61-88, <https://doi.org/10.1016/j.earscirev.2014.08.002>

- [4] E.K. Tschegg, A. Schneemayer, I. Merta, K.A. Rieder, Energy dissipation capacity of fibre reinforced concrete under biaxial tension–compression load. Part I: Test equipment and work of fracture, *Cement and Concrete Composites* 62 (2015) 195-203, <https://doi.org/10.1016/j.cemconcomp.2015.07.002>
- [5] H. Wang, L. Wang, Y. Song, J. Wang, Influence of free water on dynamic behavior of dam concrete under biaxial compression, *Construction and Building Materials* 112 (2016) 222-231, <https://doi.org/10.1016/j.conbuildmat.2016.02.090>
- [6] S. Arora, B. Mishra, Investigation of the failure mode of shale rocks in biaxial and triaxial compression tests, *International Journal of Rock Mechanics and Mining Sciences* 79 (2015) 109-123, <https://doi.org/10.1016/j.ijrmms.2015.08.014>
- [7] J.L.H. Cailteux, P. Muchez, J. De Cuyper, S. Dewaele, T. De Putter, Origin of the megabreccias in the Katanga Copperbelt (D.R.Congo), *Journal of African Earth Sciences* 140 (2018) 76-93, <https://doi.org/10.1016/j.jafrearsci.2017.12.029>
- [8] T.H. Heaton, J.F. Hall, D.J. Wald, M.W. Halling, Response of High-Rise and Base-Isolated Buildings to a Hypothetical Mw 7.0 Blind Thrust Earthquake, *Science* 267(5195) (1995) 206, <https://doi.org/10.1126/science.267.5195.206>
- [9] A. Mazaira, P. Konicek, Intense rockburst impacts in deep underground construction and their prevention, *Canadian Geotechnical Journal* 52(10) (2015) 1426-1439, <https://doi.org/10.1139/cgj-2014-0359>
- [10] B.S. Butler, G.F. Loughlin, V.C. Heikes, *Ore Deposits of Utah*, U.S. Government Printing Office 1920, <https://doi.org/10.3133/pp111>
- [11] J.P. Ingham, 5 - Concrete, in: J.P. Ingham (Ed.), *Geomaterials Under the Microscope*, Academic Press, Boston, 2013, pp. 75-120, <https://doi.org/10.1016/B978-0-12-407230-5.50013-3>
- [12] A.V. Nikiforov, H. Öztürk, S. Altuncu, V.A. Lebedev, Kizilcaören ore-bearing complex with carbonatites (northwestern Anatolia, Turkey): Formation time and mineralogy of rocks, *Geology of Ore Deposits* 56(1) (2014) 35-60, <https://doi.org/10.1134/s107570151401005x>
- [13] H. Lan, C.D. Martin, B. Hu, Effect of heterogeneity of brittle rock on micromechanical extensile behavior during compression loading, *Journal of Geophysical Research: Solid Earth* 115(B1) (2010), <https://doi.org/10.1029/2009jb006496>
- [14] M.C. Villeneuve, M.S. Diederichs, P.K. Kaiser, Effects of Grain Scale Heterogeneity on Rock Strength and the Chipping Process, *International Journal of Geomechanics* 12(6) (2012) 632-647, [https://doi.org/doi:10.1061/\(ASCE\)GM.1943-5622.0000194](https://doi.org/doi:10.1061/(ASCE)GM.1943-5622.0000194)
- [15] X.F. Li, Q.B. Zhang, H.B. Li, J. Zhao, Grain-Based Discrete Element Method (GB-DEM) Modelling of Multi-scale Fracturing in Rocks Under Dynamic Loading, *Rock Mechanics and Rock Engineering* (2018), <https://doi.org/10.1007/s00603-018-1566-2>
- [16] C.A. Tang, H. Liu, P.K.K. Lee, Y. Tsui, L.G. Tham, Numerical studies of the influence of microstructure on rock failure in uniaxial compression — Part I: effect of heterogeneity, *International Journal of Rock Mechanics and Mining Sciences* 37(4) (2000) 555-569, [https://doi.org/10.1016/S1365-1609\(99\)00121-5](https://doi.org/10.1016/S1365-1609(99)00121-5)
- [17] Q.B. Zhang, J. Zhao, Effect of loading rate on fracture toughness and failure micromechanisms in marble, *Engineering Fracture Mechanics* 102 (2013) 288-309, <https://doi.org/10.1016/j.engfracmech.2013.02.009>
- [18] E. Piotrowska, P. Forquin, Y. Malecot, Experimental study of static and dynamic behavior of concrete under high confinement: Effect of coarse aggregate strength, *Mechanics of Materials* 92 (2016) 164-174, <https://doi.org/10.1016/j.mechmat.2015.09.005>

- [19] K.-M. Kim, S. Lee, J.-Y. Cho, Effect of maximum coarse aggregate size on dynamic compressive strength of high-strength concrete, *International Journal of Impact Engineering* 125 (2019) 107-116, <https://doi.org/10.1016/j.ijimpeng.2018.11.003>
- [20] J. Wastiels, Behaviour of concrete under multiaxial stresses—a review, *Cement and Concrete Research* 9(1) (1979) 35-44, [https://doi.org/10.1016/0008-8846\(79\)90092-9](https://doi.org/10.1016/0008-8846(79)90092-9)
- [21] Q.B. Zhang, J. Zhao, A Review of Dynamic Experimental Techniques and Mechanical Behaviour of Rock Materials, *Rock Mechanics and Rock Engineering* 47(4) (2014) 1411-1478, <https://doi.org/10.1007/s00603-013-0463-y>
- [22] M.R. Khosravani, K. Weinberg, A review on split Hopkinson bar experiments on the dynamic characterisation of concrete, *Construction and Building Materials* 190 (2018) 1264-1283, <https://doi.org/10.1016/j.conbuildmat.2018.09.187>
- [23] R.J. Christensen, S.R. Swanson, W.S. Brown, Split-hopkinson-bar tests on rock under confining pressure, *Experimental Mechanics* 12(11) (1972) 508-513, <https://doi.org/10.1007/BF02320747>
- [24] U.S. Lindholm, L.M. Yeakley, A. Nagy, The dynamic strength and fracture properties of dresser basalt, *International Journal of Rock Mechanics and Mining Sciences & Geomechanics Abstracts* 11(5) (1974) 181-191, [https://doi.org/10.1016/0148-9062\(74\)90885-7](https://doi.org/10.1016/0148-9062(74)90885-7)
- [25] A.L.F. J.K. Gran, J.D. Colton, Dynamic triaxial tests of high-strength concrete, *J. Eng. Mech.* 115 (1989) 891–904 (1989),
- [26] L.E. Malvern, D.A.L. Jenkins, Dynamic Testing of Laterally Confined Concrete, In: *Micromechanics of failure of quasi brittle materials.*, Amsterdam: Elsevier Applied Science;, 1990, pp. 343-52.
- [27] K. Fujikake, *Dynamic Properties Of Concrete Materials With High Rates Of Tri-axial Compressive Loads*, (2000),
- [28] X. Li, Z. Zhou, T.-S. Lok, L. Hong, T. Yin, Innovative testing technique of rock subjected to coupled static and dynamic loads, *International Journal of Rock Mechanics and Mining Sciences* 45(5) (2008) 739-748, <https://doi.org/10.1016/j.ijrmms.2007.08.013>
- [29] G. Chen, Y.C. Kuang, X.C. Huang, A.M. Xu, Dynamic Compressive Behavior of Granite under Active Confinement, *Advanced Materials Research* 291-294 (2011) 1227-1232, <https://doi.org/10.4028/www.scientific.net/AMR.291-294.1227>
- [30] J. Jin, X. Li, G. Wang, Z. Yin, Failure modes and mechanisms of sandstone under cyclic impact loadings, *Journal of Central South University (Science and Technology)* 43(4) (2012) 1453-1461,
- [31] Q. Zhang, *Mechanical Behaviour of Rock Materials under Dynamic Loading*, EPFL, 2014.
- [32] J.C. Gong, L.E. Malvern, Passively confined tests of axial dynamic compressive strength of concrete, *Experimental Mechanics* 30(1) (1990) 55-59, <https://doi.org/10.1007/BF02322703>
- [33] P. Forquin, G. Gary, F. Gatuingt, A testing technique for concrete under confinement at high rates of strain, *International Journal of Impact Engineering* 35(6) (2008) 425-446, <https://doi.org/10.1016/j.ijimpeng.2007.04.007>
- [34] Y. Xiao, J. Shan, Q. Zheng, B. Chen, Y. Shen, Experimental Studies on Concrete Filled Steel Tubes under High Strain Rate Loading, *Journal of Materials in Civil Engineering* 21(10) (2009) 569-577, [https://doi.org/doi:10.1061/\(ASCE\)0899-1561\(2009\)21:10\(569\)](https://doi.org/doi:10.1061/(ASCE)0899-1561(2009)21:10(569))

- [35] F. Yuan, V. Prakash, T. Tullis, Origin of pulverized rocks during earthquake fault rupture, *Journal of Geophysical Research: Solid Earth* 116(B6) (2011), <https://doi.org/10.1029/2010jb007721>
- [36] P. Bailly, F. Delvare, J. Vial, J.L. Hanus, M. Biessy, D. Picart, Dynamic behavior of an aggregate material at simultaneous high pressure and strain rate: SHPB triaxial tests, *International Journal of Impact Engineering* 38(2) (2011) 73-84, <https://doi.org/https://doi.org/10.1016/j.ijimpeng.2010.10.005>
- [37] K. Mogi, Effect of the triaxial stress system on the failure of dolomite and limestone, *Tectonophysics* 11(2) (1971) 111-127, [https://doi.org/10.1016/0040-1951\(71\)90059-X](https://doi.org/10.1016/0040-1951(71)90059-X)
- [38] G.L. Dongming Yan, C. Genda, Dynamic Properties of Plain Concrete in Triaxial Stress State, *ACI Materials Journal* 106(1) (2009), <https://doi.org/10.14359/56321>
- [39] Y. Zhang, X.-T. Feng, X. Zhang, Z. Wang, M. Sharifzadeh, C. Yang, A Novel Application of Strain Energy for Fracturing Process Analysis of Hard Rock Under True Triaxial Compression, *Rock Mechanics and Rock Engineering* 52(11) (2019) 4257-4272, <https://doi.org/10.1007/s00603-019-01868-8>
- [40] P. Sukontasukkul, S. Mindess, N. Banthia, Properties of confined fibre-reinforced concrete under uniaxial compressive impact, *Cement and Concrete Research* 35(1) (2005) 11-18, <https://doi.org/10.1016/j.cemconres.2004.05.011>
- [41] S.J. Green, J.D. Leasia, R.D. Perkins, A.H. Jones, Triaxial stress behavior of Solenhofen limestone and westerly granite at high strain rates, *Journal of Geophysical Research (1896-1977)* 77(20) (1972) 3711-3724, <https://doi.org/10.1029/JB077i020p03711>
- [42] H.K.H. Helmut Kupfer, R. Hubert, Behavior of Concrete Under Biaxial Stresses, *ACI Journal Proceedings* 66(8) (1969), <https://doi.org/10.14359/7388>
- [43] B. Amadei, V. Janoo, M. Robison, R. Kuberan, Strength Of Indiana Limestone In True Biaxial Loading Conditions, *The 25th U.S. Symposium on Rock Mechanics (USRMS)*, American Rock Mechanics Association, Evanston, Illinois, 1984, p. 11.
- [44] A. Bobet, H.H. Einstein, Fracture coalescence in rock-type materials under uniaxial and biaxial compression, *International Journal of Rock Mechanics and Mining Sciences* 35(7) (1998) 863-888, [https://doi.org/10.1016/S0148-9062\(98\)00005-9](https://doi.org/10.1016/S0148-9062(98)00005-9)
- [45] D. Yan, S. Xu, G. Chen, H. Li, Biaxial behaviour of plain concrete subjected to dynamic compression with constant lateral stress, *Structural Concrete* 15(2) (2014) 202-209, <https://doi.org/10.1002/suco.201300057>
- [46] M. Quast, M. Curbach, Concrete under biaxial dynamic compressive loading, *Procedia Engineering* 210 (2017) 24-31, <https://doi.org/10.1016/j.proeng.2017.11.044>
- [47] J. Weerheijm, H.W. Reinhardt, Biaxial Loading Device for Dynamic Concrete Response, *Le Journal de Physique Colloques* 49(C3) (1988) C3-733-C3-738, <https://doi.org/10.1051/jphyscol:19883104>
- [48] B. Paliwal, K.T. Ramesh, J.W. McCauley, M. Chen, Dynamic Compressive Failure of AlON Under Controlled Planar Confinement, *Journal of the American Ceramic Society* 91(11) (2008) 3619-3629, <https://doi.org/10.1111/j.1551-2916.2008.02712.x>
- [49] E. Cadoni, M. Dotta, D. Forni, G. Riganti, C. Albertini, First application of the 3D-MHB on dynamic compressive behavior of UHPC, *EPJ Web of Conferences* 94 (2015), <https://doi.org/10.1051/epjconf/20159401031>

- [50] K. Liu, Q. Zhang, G. Wu, J. Li, J. Zhao, Dynamic mechanical and fracture behaviour of sandstone under multiaxial loads using a triaxial hopkinson bar, *Rock Mechanics and Rock Engineering* 52(7) (2019) 2175-2195, <https://doi.org/10.1007/s00603-018-1691>
- [51] K. Liu, J. Zhao, G. Wu, A. Maksimenko, A. Haque, Q.B. Zhang, Dynamic strength and failure modes of sandstone under biaxial compression, *International Journal of Rock Mechanics and Mining Sciences* 128 (2020), <https://doi.org/10.1016/j.ijrmms.2020.104260>
- [52] P. Liu, K. Liu, Q.B. Zhang, Experimental characterisation of mechanical behaviour of concrete-like materials under multiaxial confinement and high strain rate, *Construction and Building Materials* 258 (2020), <https://doi.org/10.1016/j.conbuildmat.2020.119638>
- [53] S. Xu, J. Shan, L. Zhang, L. Zhou, G. Gao, S. Hu, P. Wang, Dynamic compression behaviors of concrete under true triaxial confinement: An experimental technique, *Mechanics of Materials* 140 (2020), <https://doi.org/10.1016/j.mechmat.2019.103220>
- [54] Q.B. Zhang, K. Liu, G. Wu, J. Zhao, Dynamic Deformation, Damage, and Fracture in Geomaterials, *Handbook of Damage Mechanics*, Springer, New York, NY, 2021, pp. 1-44, https://doi.org/10.1007/978-1-4614-8968-9_73-1
- [55] E. Sahouryeh, A.V. Dyskin, L.N. Germanovich, Crack growth under biaxial compression, *Engineering Fracture Mechanics* 69(18) (2002) 2187-2198, [https://doi.org/10.1016/S0013-7944\(02\)00015-2](https://doi.org/10.1016/S0013-7944(02)00015-2)
- [56] C. Zou, L.N.Y. Wong, J.J. Loo, B.S. Gan, Different mechanical and cracking behaviors of single-flawed brittle gypsum specimens under dynamic and quasi-static loadings, *Engineering Geology* 201 (2016) 71-84, <https://doi.org/10.1016/j.enggeo.2015.12.014>
- [57] Q.B. Zhang, J. Zhao, Determination of mechanical properties and full-field strain measurements of rock material under dynamic loads, *International Journal of Rock Mechanics and Mining Sciences* 60 (2013) 423-439, <https://doi.org/10.1016/j.ijrmms.2013.01.005>
- [58] G. Gao, S. Huang, K. Xia, Z. Li, Application of Digital Image Correlation (DIC) in Dynamic Notched Semi-Circular Bend (NSCB) Tests, *Experimental Mechanics* 55(1) (2015) 95-104, <https://doi.org/10.1007/s11340-014-9863-5>
- [59] G. Gao, W. Yao, K. Xia, Z. Li, Investigation of the rate dependence of fracture propagation in rocks using digital image correlation (DIC) method, *Engineering Fracture Mechanics* 138 (2015) 146-155, <https://doi.org/10.1016/j.engfracmech.2015.02.021>
- [60] P.F. Luo, Y.J. Chao, M.A. Sutton, W.H. Peters, Accurate measurement of three-dimensional deformations in deformable and rigid bodies using computer vision, *Experimental Mechanics* 33(2) (1993) 123-132, <https://doi.org/10.1007/BF02322488>
- [61] A.S. Michael, J.H. Yan, D. Xiaomin, C.S. Cheng, P. Zavattieri, Three-dimensional digital image correlation to quantify deformation and crack-opening displacement in ductile aluminum under mixed-mode I/III loading, *Optical Engineering* 46(5) (2007) 1-17, <https://doi.org/10.1117/1.2741279>
- [62] M.A. Sutton, J.J. Ortu, H. Schreier, Image correlation for shape, motion and deformation measurements: basic concepts, theory and applications, Springer Science & Business Media 2009, <https://doi.org/10.1007/978-0-387-78747-3>
- [63] H.Z. Xing, Q.B. Zhang, D. Ruan, S. Dehkoda, G.X. Lu, J. Zhao, Full-field measurement and fracture characterisations of rocks under dynamic loads using high-speed three-dimensional digital image correlation, *International Journal of Impact Engineering* 113 (2018) 61-72, <https://doi.org/10.1016/j.ijimpeng.2017.11.011>

- [64] B. Oliver, B. Kathleen, D. Susanne, M. Bert, D. Tilman, H. Julia, B. Felix, Comparison between x-ray tube-based and synchrotron radiation-based μ CT, Proc.SPIE, 2008.
- [65] R.A. Johns, J.S. Steude, L.M. Castanier, P.V. Roberts, Nondestructive measurements of fracture aperture in crystalline rock cores using X ray computed tomography, Journal of Geophysical Research: Solid Earth 98(B2) (1993) 1889-1900, <https://doi.org/10.1029/92jb02298>
- [66] V. Cnudde, A. Cwirzen, B. Masschaele, P.J.S. Jacobs, Porosity and microstructure characterization of building stones and concretes, Engineering Geology 103(3) (2009) 76-83, <https://doi.org/10.1016/j.enggeo.2008.06.014>
- [67] K. Van Tittelboom, N. De Belie, D. Van Loo, P. Jacobs, Self-healing efficiency of cementitious materials containing tubular capsules filled with healing agent, Cement and Concrete Composites 33(4) (2011) 497-505, <https://doi.org/j.cemconcomp.2011.01.004>
- [68] C. Madonna, B. Quintal, M. Frehner, B.S. Almqvist, N. Tisato, M. Pistone, F. Marone, E.H. Saenger, Synchrotron-based X-ray tomographic microscopy for rock physics investigations Synchrotron-based rock images, Geophysics 78(1) (2013) D53-D64, <https://doi.org/10.1190/geo2012-0113.1>
- [69] L.G. Ugarriza, E. Saber, S.R. Vantaram, V. Amuso, M. Shaw, R. Bhaskar, Automatic image segmentation by dynamic region growth and multiresolution merging, IEEE transactions on image processing 18(10) (2009) 2275-2288, <https://doi.org/10.1109/TIP.2009.2025555>
- [70] S. Schlüter, A. Sheppard, K. Brown, D. Wildenschild, Image processing of multiphase images obtained via X - ray microtomography: a review, Water Resources Research 50(4) (2014) 3615-3639, <https://doi.org/10.1002/2014WR015256>
- [71] O.Z. Kraus, J.L. Ba, B.J. Frey, Classifying and segmenting microscopy images with deep multiple instance learning, Bioinformatics 32(12) (2016) i52-i59, <https://doi.org/10.1093/bioinformatics/btw252>
- [72] L. Zhang, L. Zhang, B. Du, Deep Learning for Remote Sensing Data: A Technical Tutorial on the State of the Art, IEEE Geoscience and Remote Sensing Magazine 4(2) (2016) 22-40, <https://doi.org/10.1109/MGRS.2016.2540798>
- [73] J.-G. Lee, S. Jun, Y.-W. Cho, H. Lee, G.B. Kim, J.B. Seo, N. Kim, Deep Learning in Medical Imaging: General Overview, Korean journal of radiology 18(4) (2017) 570-584, <https://doi.org/10.3348/kjr.2017.18.4.570>
- [74] C. Ly, A.M. Olsen, I.J. Schwerdt, R. Porter, K. Sentz, L.W. McDonald, T. Tasdizen, A new approach for quantifying morphological features of U3O8 for nuclear forensics using a deep learning model, Journal of Nuclear Materials 517 (2019) 128-137, <https://doi.org/10.1016/j.jnucmat.2019.01.042>
- [75] N. Borodinov, S. Neumayer, S.V. Kalinin, O.S. Ovchinnikova, R.K. Vasudevan, S. Jesse, Deep neural networks for understanding noisy data applied to physical property extraction in scanning probe microscopy, npj Computational Materials 5(1) (2019) 25, <https://doi.org/10.1038/s41524-019-0148-5>
- [76] Y. Toda, F. Okura, J. Ito, S. Okada, T. Kinoshita, H. Tsuji, D. Saisho, Training instance segmentation neural network with synthetic datasets for crop seed phenotyping, Communications Biology 3(1) (2020) 173, <https://doi.org/10.1038/s42003-020-0905-5>
- [77] T. Özturan, C. Çeçen, Effect of coarse aggregate type on mechanical properties of concretes with different strengths, Cement and Concrete Research 27(2) (1997) 165-170, [https://doi.org/10.1016/S0008-8846\(97\)00006-9](https://doi.org/10.1016/S0008-8846(97)00006-9)

- [78] C. Rong, Q. Shi, T. Zhang, H. Zhao, New failure criterion models for concrete under multiaxial stress in compression, *Construction and Building Materials* 161 (2018) 432-441, <https://doi.org/10.1016/j.conbuildmat.2017.11.106>
- [79] A.C. C192M-19, Standard Practice for Making and Curing Concrete Test Specimens in the Laboratory, ASTM International, West Conshohocken, PA, 2019, www.astm.org, https://doi.org/10.1520/C0192_C0192M-19
- [80] A.C. C109M-20a, Standard Test Method for Compressive Strength of Hydraulic Cement Mortars (Using 2-in. or [50-mm] Cube Specimens), ASTM International, West Conshohocken, PA, 2020, www.astm.org, https://doi.org/10.1520/C0109_C0109M-20A
- [81] C. Zou, L.N.Y. Wong, Size and Geometry Effects on the Mechanical Properties of Carrara Marble Under Dynamic Loadings, *Rock Mechanics and Rock Engineering* 49(5) (2016) 1695-1708, <https://doi.org/10.1007/s00603-015-0899-3>
- [82] H. Kolsky, An Investigation of the Mechanical Properties of Materials at very High Rates of Loading, *Proceedings of the Physical Society. Section B* 62(11) (1949) 676-700, <https://doi.org/10.1088/0370-1301/62/11/302>
- [83] C. Hall, D. Hausermann, A. Maksimenko, A. Astolfo, K. Siu, J. Pearson, A. Stevenson, Detectors for the Imaging and Medical Beam Line at the Australian Synchrotron, *Journal of Instrumentation* 8(06) (2013) C06011-C06011, <https://doi.org/10.1088/1748-0221/8/06/c06011>
- [84] J. Schindelin, I. Arganda-Carreras, E. Frise, V. Kaynig, M. Longair, T. Pietzsch, S. Preibisch, C. Rueden, S. Saalfeld, B. Schmid, J.-Y. Tinevez, D.J. White, V. Hartenstein, K. Eliceiri, P. Tomancak, A. Cardona, Fiji: an open-source platform for biological-image analysis, *Nature Methods* 9(7) (2012) 676-682, <https://doi.org/10.1038/nmeth.2019>
- [85] M. Hall, E. Frank, G. Holmes, B. Pfahringer, P. Reutemann, I.H. Witten, The WEKA data mining software: an update, *SIGKDD Explor. Newsl.* 11(1) (2009) 10–18, <https://doi.org/10.1145/1656274.1656278>
- [86] D.F. Polan, S.L. Brady, R.A. Kaufman, Tissue segmentation of computed tomography images using a Random Forest algorithm: a feasibility study, *Phys Med Biol* 61(17) (2016) 6553-6569, <https://doi.org/10.1088/0031-9155/61/17/6553>
- [87] I. Arganda-Carreras, V. Kaynig, C. Rueden, K.W. Eliceiri, J. Schindelin, A. Cardona, H. Sebastian Seung, Trainable Weka Segmentation: a machine learning tool for microscopy pixel classification, *Bioinformatics* 33(15) (2017) 2424-2426, <https://doi.org/10.1093/bioinformatics/btx180>
- [88] B. Chiaia, J.G.M. van Mier, A. Vervuurt, Crack Growth Mechanisms in Four Different Concretes: Microscopic Observations and Fractal Analysis, *Cement and Concrete Research* 28(1) (1998) 103-114, [https://doi.org/10.1016/S0008-8846\(97\)00221-4](https://doi.org/10.1016/S0008-8846(97)00221-4)
- [89] M.A. Issa, M.A. Issa, M.S. Islam, A. Chudnovsky, Fractal dimension—a measure of fracture roughness and toughness of concrete, *Engineering Fracture Mechanics* 70(1) (2003) 125-137, [https://doi.org/10.1016/S0013-7944\(02\)00019-X](https://doi.org/10.1016/S0013-7944(02)00019-X)
- [90] O.K. Mahabadi, B.S.A. Tatone, G. Grasselli, Influence of microscale heterogeneity and microstructure on the tensile behavior of crystalline rocks, *Journal of Geophysical Research: Solid Earth* 119(7) (2014) 5324-5341, <https://doi.org/10.1002/2014jb011064>
- [91] M. Zhang, H.J. Wu, Q.M. Li, F.L. Huang, Further investigation on the dynamic compressive strength enhancement of concrete-like materials based on split Hopkinson pressure bar tests. Part I: Experiments,

International Journal of Impact Engineering 36(12) (2009) 1327-1334,
<https://doi.org/10.1016/j.ijimpeng.2009.04.009>

[92] E.A. Flores-Johnson, Q.M. Li, Structural effects on compressive strength enhancement of concrete-like materials in a split Hopkinson pressure bar test, International Journal of Impact Engineering 109 (2017) 408-418, <https://doi.org/10.1016/j.ijimpeng.2017.08.003>

[93] C.Y. Li, S.J. Chen, W.G. Li, X.Y. Li, D. Ruan, W.H. Duan, Dynamic increased reinforcing effect of graphene oxide on cementitious nanocomposite, Construction and Building Materials 206 (2019) 694-702, <https://doi.org/10.1016/j.conbuildmat.2019.02.001>

[94] P.H. Bischoff, S.H. Perry, Compressive behaviour of concrete at high strain rates, Materials and Structures 24(6) (1991) 425-450, <https://doi.org/10.1007/BF02472016>

[95] M.Y.H. Bangash, Concrete and concrete structures : numerical modelling and applications, Elsevier Applied Science, London; New York, 1989, [https://doi.org/10.1016/0958-9465\(90\)90023-q](https://doi.org/10.1016/0958-9465(90)90023-q)

[96] B. Lundberg, A split Hopkinson bar study of energy absorption in dynamic rock fragmentation, International Journal of Rock Mechanics and Mining Sciences & Geomechanics Abstracts 13(6) (1976) 187-197, [https://doi.org/10.1016/0148-9062\(76\)91285-7](https://doi.org/10.1016/0148-9062(76)91285-7)

[97] Z. Zhang, An empirical relation between mode I fracture toughness and the tensile strength of rock, International Journal of Rock Mechanics and Mining Sciences 39(3) (2002) 401-406, [https://doi.org/10.1016/s1365-1609\(02\)00032-1](https://doi.org/10.1016/s1365-1609(02)00032-1)

[98] R.O. Ritchie, The conflicts between strength and toughness, Nature Materials 10(11) (2011) 817-822, <https://doi.org/10.1038/nmat3115>

[99] K. Man, X. Liu, Dynamic Fracture Toughness and Dynamic Tensile Strength of the Rock from Different Depths of Beijing Datai Well, Advances in Civil Engineering 2018 (2018) 2567438, <https://doi.org/10.1155/2018/2567438>